inorganics

MDPI

Article

The Use of Rapid Precipitation to Synthesise Multivariate UiO-66 Metal–Organic Frameworks for Photocatalysis

Ehsan Ezzatpour Ghadim [1], Marc Walker [2] and Richard I. Walton [1,*]

[1] Department of Chemistry, University of Warwick, Coventry CV4 7AL, UK; ehsan.ghadim@warwick.ac.uk
[2] Department of Physics, University of Warwick, Coventry CV4 7AL, UK; m.walker@warwick.ac.uk
* Correspondence: r.i.walton@warwick.ac.uk

Abstract: A rapid synthesis method is used to form multivariate metal–organic frameworks (MTV-MOFs) with the UiO-66 structure, where precipitation occurs upon mixing solutions of ligands and metal salts at temperatures less than 60 °C. The materials include mixtures of metals and ligands, Ce/Zr-UiO-66(1,4-NDC/BDC), Ce/Zr-UiO-66(1,4-NDC/2,6-NDC), Ce/Zr-UiO-66(1,4-NDC), Ce/Ti-UiO-66(1,4-NDC), and Ce/Ti-UiO-66(BDC-NH_2) (NDC = naphthalene dicarboxylate, BDC = benzene-1,4-dicarboxylate, BDC-NH_2 = 2-amino-benzene-1,4-dicarboxylate). Phase purity was determined by powder X-ray diffraction (PXRD), with a broadening of the profile indicative of nanoscale crystallites, verified by scanning electron microscopy (SEM). The molar ratio of metals and organic ligands in Ce/Zr-UiO-66(1,4-NDC/2,6-NDC) was confirmed by X-ray fluorescence (XRF) and solution ^{1}H nuclear magnetic resonance (NMR) after digestion, respectively. Analysis of the adsorption of dyes by the MTV-MOFs showed that a pseudo-first-order model accounts for the kinetics. The effectiveness of photocatalytic degradation of two cationic (methylene blue and rhodamine B) and two anionic (Congo red and Alizarin Red S (AR)) dyes was studied under UV and visible light. The most effective photocatalytic degradation was found between 1 and 15 min towards both cationic and anionic dyes by Ce/Zr-UiO-66(1,4-NDC/2,6-NDC). Measurements of recyclability and photostability showed retention of crystallinity after five cycles of use and exposure to light for 17 h, as confirmed by PXRD.

Keywords: UiO-66; MTV-MOFs; photocatalytic activities; rapid synthesis precipitation

Citation: Ezzatpour Ghadim, E.; Walker, M.; Walton, R.I. The Use of Rapid Precipitation to Synthesise Multivariate UiO-66 Metal–Organic Frameworks for Photocatalysis. *Inorganics* **2023**, *11*, 455. https://doi.org/10.3390/inorganics11120455

Academic Editors: Richard Dronskowski, Christian Julien, Rainer Niewa, Guido Kickelbick, Alexander S. Novikov, Gary Hix and Hans-Conrad zur Loye

Received: 18 September 2023
Revised: 1 November 2023
Accepted: 15 November 2023
Published: 24 November 2023

1. Introduction

In recent decades, metal–organic frameworks (MOFs) have been synthesized with the stability, high surface area, and porosity needed for practical applications such as gas adsorption, heterogeneous catalysis, water purification, and photocatalytic degradation [1,2]. Multivariate MOFs (MTV-MOFs) are formed from mixed metals and/or mixed linkers within the same framework topology, much like solid solutions in traditional solids, and this gives additional control over functionality [3]. UiO-66(Zr) (UiO = Universitetet i Oslo) is the parent of a set of isoreticular materials that has received tremendous attention for a large range of potential practical applications. In the parent UiO-66 structure, tetravalent metals such as Zr, Ce, Ti and Hf are present in hexanuclear oxo-clusters 12-fold coordinated to benzene-1,4-dicarboxylate (BDC) linkers to give the ideal composition $M_6O_4(OH)_4(BDC)_6$ [4]. Among these tetravalent metal ions, Ce and Ti give promising candidate materials that can be used for photocatalytic degradation applications in single- or mixed-metal forms of UiO-66 [5].

Ce(IV) has unoccupied low-lying 4f orbitals and two oxidation states (III, IV) that can be interconverted in different chemical environments [6]. Unoccupied 4f orbitals are able to participate in ligand to metal charge transfer (LMCT) and facilitate the transfer of photogenerated electrons, leading to a minimum rate of electron–hole recombination [7]. Adding a second metal to the oxo-cluster maintains the photogenerated electron for a longer time by using lattice oxygen (O_{latt}) to facilitate the internal redox cycle between the

metals within the ground and excited states [8]. For example, Ti(IV) with low-lying empty 3d orbitals can be used to accelerate the reversible redox between Ce(III) and Ce(IV) [9]. Based on recent studies, Zr in UiO-66 has mostly been used to provide structural stability, rather than playing a role in redox cycles [10].

The purpose of using chromophores in photocatalysts is to increase the photon response under exposure to different wavelengths in both the UV and visible regions of light [11]. An amino-modified linker has been used for this purpose, and works as a strong antenna to absorb the photon energy of light (E_{abs}) and shift it to the visible region (above 350 nm), with a red-shifted absorption edge, giving a narrower band gap [12,13]. In fact, the position and value of valence and conduction bands can be tuned by the use of electron-donating and -withdrawing groups on the linkers, such as amino [5]. Some linkers such as 2,6-naphthalenedicarboxylate (2,6-NDC) are photoluminescent and can be triggered for a longer time compared to simple linkers (such as 1,4-benzenedicarboxylate (BDC)) under light irradiation; they can also adjust the E_{abs} to above 350 nm [14]. Photodegradation is an oxidation process under light irradiation that can be used to break down dyes into non-toxic products such as CO_2 and H_2O, as shown in recent works on MOF photocatalysts [15,16].

There are various methods to synthesize Ce(IV) MOFs that contain linkers with different functionalities, such as by exchanging ligands by a post-synthesis method or liquid-assisted grinding [17,18]. There are some limitations in the synthesis of MOFs that contain linkers with reactive functional groups, such as the amino group that can be oxidized by Ce(IV) during the formation of the MOF [19]. Regarding the reduction in Ce(IV) during MOF formation, one strategy to minimize this possibility is to use rapid synthesis methods such as microwave heating or short reflux (15–20 min) to provide an opportunity to include as much Ce(IV) as possible before the reduction occurs [20,21].

In this work, we investigate the use of precipitation to rapidly form a new series of MTV-MOF materials with the UiO-66 structure to be studied for the photocatalytic degradation of dyes, following from our recent work that studied the formation of Ce-UiO-66 materials [22]. Herein, Ce/Zr-UiO-66(1,4-NDC/BDC), Ce/Zr-UiO-66(1,4-NDC/2,6-NDC), Ce/Zr-UiO-66(1,4-NDC), Ce/Ti-UiO-66(1,4-NDC), and Ce/Ti-UiO-66(BDC-NH_2) are formed with a high yield by mixing suitable precursor solutions. The structures of the linker precursors are shown in Figure 1. The effects of using multiple metals (Ce, Zr, and Ti) with electron-donating linkers (1,4-H_2NDC, 2,6-H_2NDC, and 1,4-H_2BDC-NH_2) are investigated for the photocatalytic degradation of both cationic (methylene blue (MB) and rhodamine B (RhB)) and anionic (Alizarine Red S (AR) and Congo red (CR)) dyes under UV and visible light irradiation at room temperature.

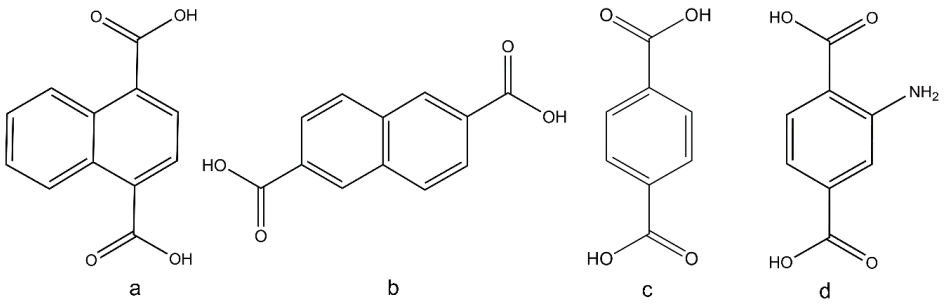

Figure 1. The acid form of the organic linkers used to prepare MTV forms of UiO-66 in this work, (**a**) 1,4-H_2NDC, (**b**) 2,6-H_2NDC, (**c**) H_2BDC, and (**d**) H_2BDC-NH_2.

2. Results

2.1. Analysis of Powder XRD

The crystalline MTV-MOFs Ce/Zr-UiO-66(1,4-NDC/BDC), Ce/Zr-UiO-66(1,4-NDC/2,6-NDC), Ce/Zr-UiO-66(1,4-NDC), Ce/Ti-UiO-66(1,4-NDC), and Ce/Ti-UiO-66(BDC-NH_2) were formed with a phase purity, confirmed by powder X-ray diffraction (PXRD)—see Figure 2a–e. The PXRD patterns were analyzed using the Pawley method and fitted using

the expected cubic unit cell for the UiO-66 structure ($Fm\bar{3}m$). Table 1 shows the fitted cubic lattice parameterand crystallite domain size as estimated by the Scherrer analysis method. Each pattern shows a broad profile due to small crystallite domain size, which is determined to be between 7 and 15 nm. The cubic lattice parameters can be compared with those of other UiO-66 materials reported in the literature. The pure Ce analogue of UiO-66 is expected to have a larger unit cell dimension than the pure Zr material, and mixed-metal materials have intermediate values [23]. The size of unit cell of Ce/Zr has been reported as 21.0652 Å for $Zr_{3.54}Ce_{2.46}$-UiO-66 by Lomachenko et al. [24], which is smaller than that of Ce/Zr-UiO-66(1,4-NDC), which was found to be 21.321 (Å) in this study, because the molar ratio of Ce is equal to that of Zr, i.e., the Ce content is higher here. The 1,4-NDC linker should give a rise to a similar unit cell parameter to the parent BDC linker; however, the 2,6-NDC linker features a larger separation between the bridging carboxylates. The size of the lattice parameter Ce/Zr-UiO-66(1,4-NDC/2,6-NDC) is 21.202 (1) Å. A previous systematic study on synthesizing Zr with these linkers (1,4-NDC/2,6-NDC) showed that the molar ratio between ligands can define the structure of this combination, which varies between UiO-66 and Dresden University of Technology (DUT-52) [25]. In this regard, a higher concentration of 1,4-NDC compared to 2,6-NDC yields the UiO-66 structure, consistent with the results here. Butova et al. reported that the size of the unit cell of Zr-UiO-66(1,4-NDC) is 20.8538(8), which is smaller than the value found in this study [26].

Ce/Zr-UiO-66(1,4-NDC/BDC) and Ce/Zr-UiO-66(1,4-NDC/2,6-NDC) were produced by a combination of two metals and linkers with equal initial molar ratios, and Ce/Zr-UiO-66(1,4-NDC), Ce/Ti-UiO-66(1,4-NDC), and Ce/Ti-UiO-66(BDC-NH_2) were formed from two metals in a similar proportion, as confirmed by X-ray fluorescence (XRF) and thermogravimetric analysis (TGA)—see Table 1. The molar ratio of linkers was measured after digestion by nuclear magnetic resonance (NMR). Most samples were found to have a moderate number of linker defects, while Ce/Zr-UiO-66(1,4-NDC/BDC) has a non-defective structure. The NMR analysis of the digested MOF shows that the molar ratio of 1,4-NDC to 2,6-NDC is 1.45 to 1 (Table 1); therefore, a higher concentration of 1,4-NDC means that the unit cell is similar to that of the UiO-66 structure—see Table 1. The material Ce/Zr-UiO-66(1,4-NDC/BDC) represents an attempt to understand the possibility of combining two linkers with similar lengths and with different metal sizes. As shown in Table 1, the size of the unit cell of Ce/Zr-UiO-66(1,4-NDC/BDC) is 21.295 Å, which is bigger than the value in Zr-UiO-66(1,4-NDC/BDC) (20.771 Å) with an equal molar ratio of linkers (1,4-NDC = BDC, 1:1), as reported by Butova et al. [27]. Therefore, adding the second metal into Zr-UiO-66 increases the size of the unit cell parameter, with a similar length of organic linkers. The molar ratio of Ce/Zr in Ce/Zr-UiO-66 (1,4-NDC), Ce/Zr-UiO-66 (1,4-NDC/2,6-NDC), and Ce/Zr-UiO-66(1,4-NDC/BDC) is equal, and the unit cell parameter in Ce/Zr-UiO-66(1,4-NDC) is 21.321(8) Å, which is bigger than that of Ce/Zr-UiO-66 in a similar molar ratio (20.9198(4) Å), as reported by Lammert et al. [23], which is likely to be because the material studied by Lammert et al. contained a lower amount of Ce(IV).

Substituting Ti in the UiO-66(Ce) structure leads to the broadening of the Bragg peaks and a shrinking of the unit cell parameter, as reported by Wang et al. [28]. Other reports show that the unit cell parameters in Ce/Ti-UiO-66 (Ce:Ti = 1:10) and Ce/Ti-UiO-66(BDC-NH_2) (Ce: Ti = 1:1.5) are 21.4179 and 21.4955(Å) [24], respectively. In contrast, the unit cell parameters of Ce/Ti-UiO-66(BDC-NH_2) (molar ratio, Ce:Ti = 3:1) and Ce/Ti-UiO-66(1,4-NDC) (molar ratio, Ce:Ti = 1:1.72) are 21.5172 and 21.5659 Å, respectively, as shown in Table 1.

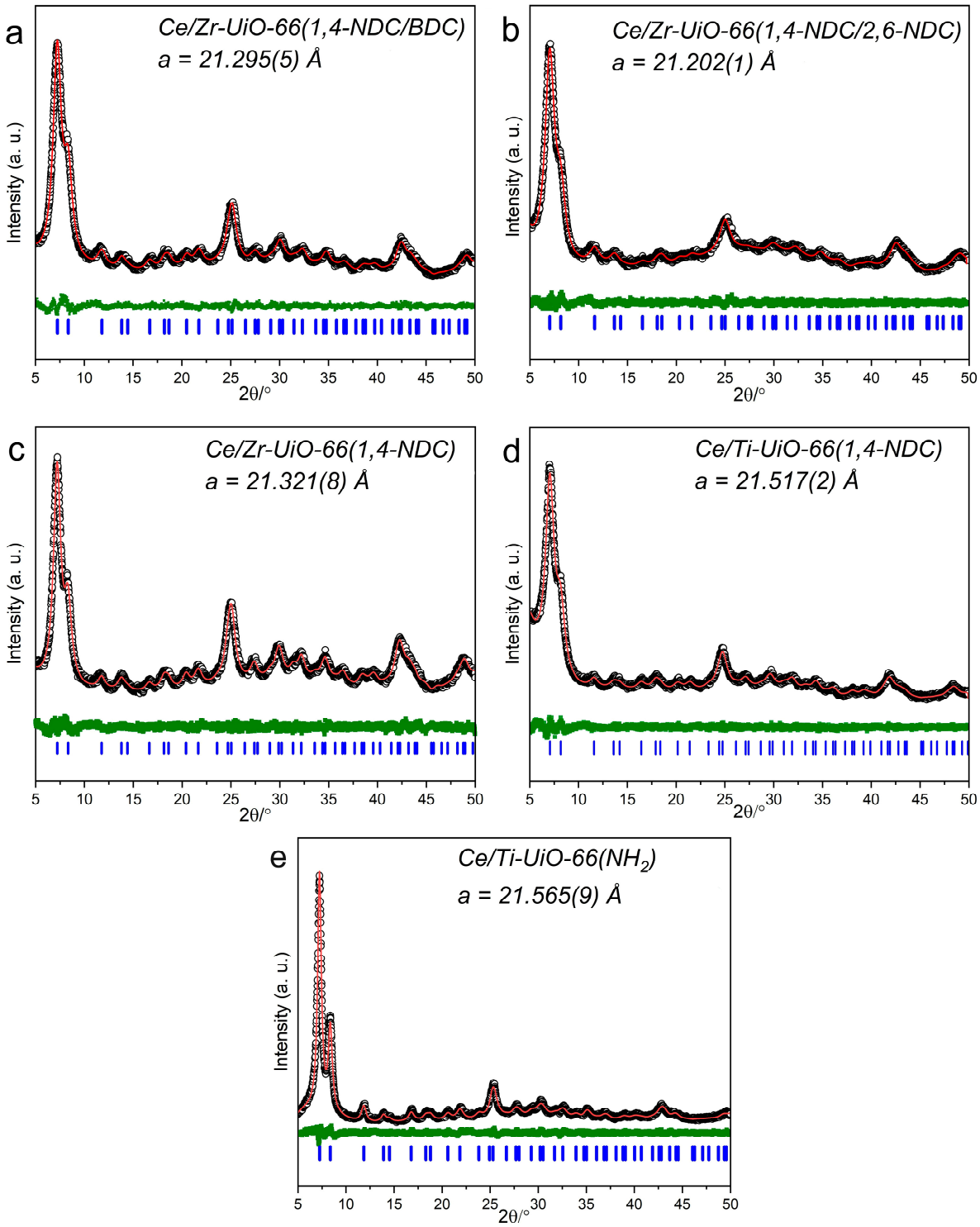

Figure 2. Fitted PXRD patterns of MTV-MOFs with the UiO-66 structure showing the experimental pattern (black points), difference plot (green), Pawley fit (red line), and allowed Bragg peak positions (blue). The space group for all samples is $Fm\bar{3}m$. (**a**) Ce/Zr-UiO-66(1,4-NDC/BDC), (**b**) Ce/Zr-UiO-66(1,4-NDC/2,6-NDC), (**c**) Ce/Zr-UiO-66(1,4-NDC), (**d**) Ce/Ti-UiO-66(1,4-NDC), (**e**) Ce/Ti-UiO-66(BDC-NH_2).

Table 1. Characterization of MTV UiO-66 materials: crystallite size, unit cell parameter from Pawley refinement against powder XRD patterns zeta potential, BET (surface area) and band gap (DR/UV-Vis). The UiO-66 chemical formula $M_6(O)_4(OH)_4(L)_6$ was determined by XRF, TGA, and digestion NMR.

Material	Crystallite Size (nm)	*a* (Å)	Zeta Potential (mV)	Surface Area (m^2g^{-1})	Band Gap (eV)
$Ce_3Zr_3(O)_4(OH)_4$(1,4-NDC)$_{2.98}$(BDC)$_{2.98}$(H_2O)$_{0.08}$	9.01 (±0.1)	21.295(5)	+18.33	250.23	2.69 ± 0.027
$Ce_3Zr_3(O)_4(OH)_4$(1,4-NDC)$_3$(2,6-NDC)$_2$(H_2O)$_{0.5}$	8.90 (±0.5)	21.202(1)	+5.50	303.61	2.08 ± 0.014
$Ce_3Zr_3(O)_4(OH)_4$(1,4-NDC)$_{5.34}$(H_2O)$_{0.33}$	9.75 (±0.1)	21.321(8)	10.56	212.32	2.00 ± 0.018
$Ce_{2.2}Ti_{3.8}(O)_4(OH)_4$(1,4-NDC)$_{4.51}$($H_2O$)$_{0.745}$	8.67 (±0.1)	21.517(2)	−4.25	136.47	1.86 ± 0.017
$Ce_{4.5}Ti_{1.5}(O)_4(OH)_4$(BDC-$NH_2$)$_{4.33}$($H_2O$)$_{0.835}$	15.12 (±0.1)	21.565(9)	4.09	144.08	2.41 ± 0.031

2.2. TGA

The TGA analysis provides information about the chemical formula and number of ligand defects per cluster. Porous materials can trap solvents, modulators, and water molecules in their pores, and they are evaporated off at between 50 and 200 °C. Water is typically evacuated between 50 and 150 °C. As shown in Figure S1, the MTV-MOFs show a mass loss at temperatures of 250–400 °C, which is related to the dehydroxylation of the metal clusters. The changes between 400 and 600 °C are due to the total combustion of the organic parts of MOFs, leading to the formation of metal oxide(s). The TGA was used to determine the number of linkers per hexameric metal cluster with the analysis method provided in the Supporting Information, and the results are shown in Table 1.

2.3. SEM Images

Freshly synthesized MTV-MOF samples were studied using SEM to minimize particle agglomeration and to observe the particles' true size and shape. This showed ultrafine nanoparticles with primary particle sizes between 10 and 30 nm, although there was a level of agglomeration that was likely due to the drying of the samples on the SEM stubs under vacuum conditions. For Ce/Zr-UiO-66(1,4 NDC/BDC), Ce/Zr-UiO-66(1,4-NDC/2,6-NDC), Ce/Zr-UiO-66(1,4-NDC), and Ce/Zr-UiO-66(1,4-NDC) nanoparticles, see Figure 3a–e. Ce/Ti-UiO-66(1,4-NDC) and Ce/Ti-UiO-66(BDC-NH_2) showed comparatively different size of particles to Ce/Zr-UiO-66(1,4-NDC/2,6-NDC) and Ce/Zr-UiO-66(1,4-NDC)—see Figure 4c,d.

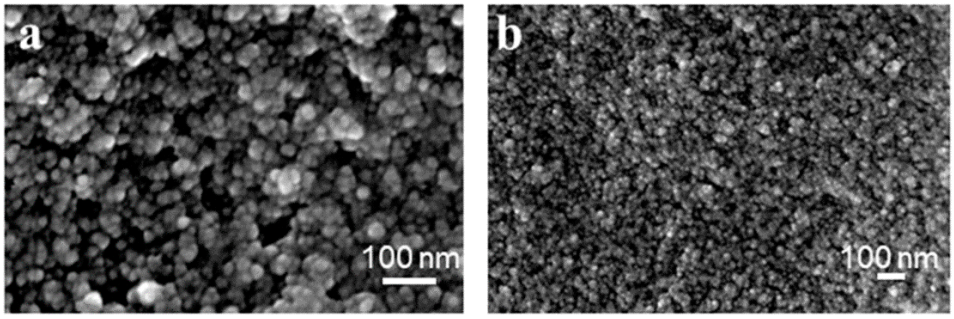

Figure 3. *Cont.*

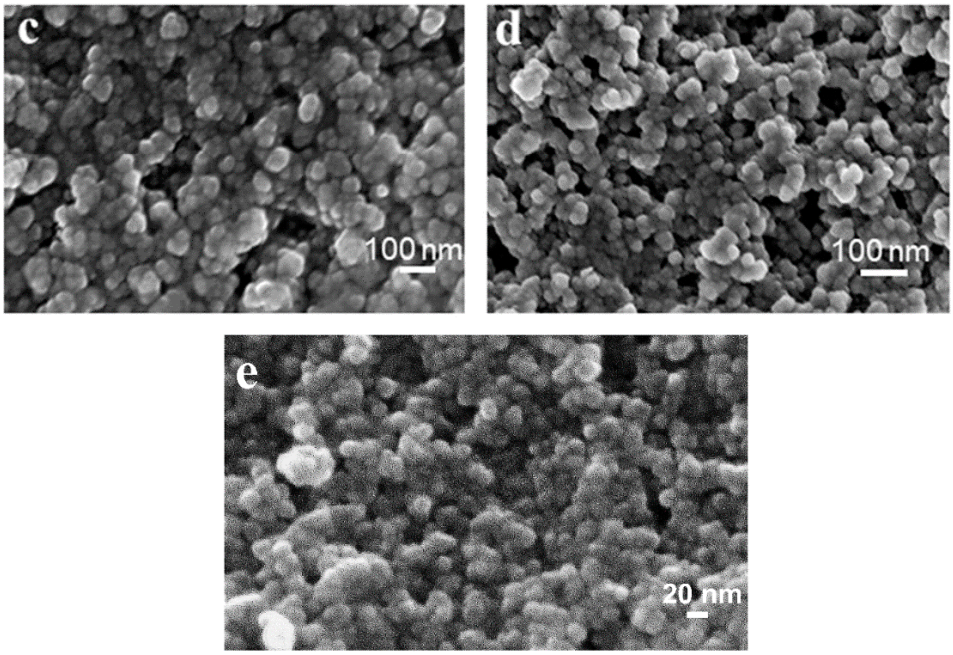

Figure 3. SEM images of (**a**) Ce/Zr-UiO-66(1,4-NDC/2,6-NDC), (**b**) Ce/Zr-UiO-66(1,4-NDC), (**c**) Ce/Ti-UiO-66(1,4-NDC), (**d**) Ce/Ti-UiO-66(-BDC-NH2), and (**e**) Ce/Zr-UiO-66(1,4-NDC/BDC).

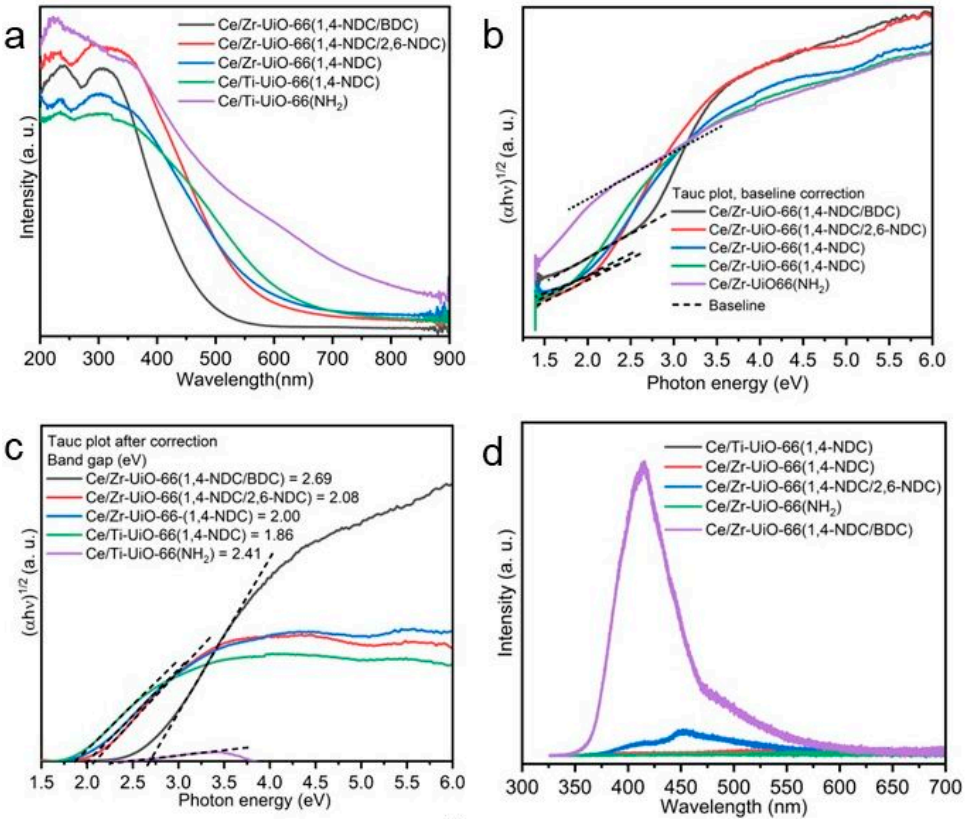

Figure 4. *Cont.*

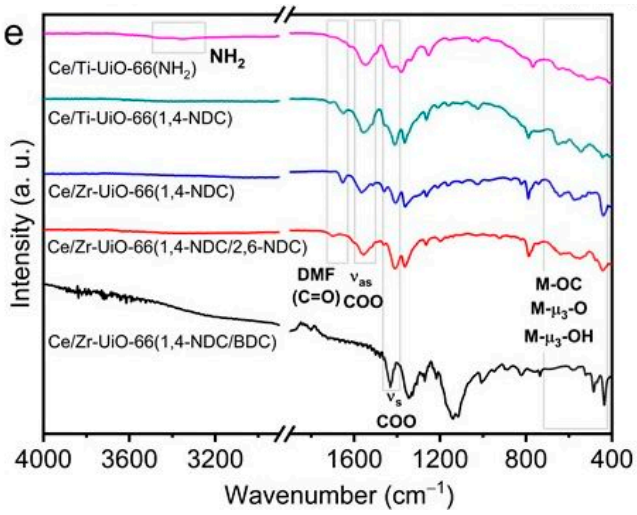

Figure 4. Analysis of Ce/Zr-UiO-66(1,4-NDC/BDC), Ce/Zr-UiO-66(1,4-NDC/2,6-NDC), Ce/Ti-UiO-66(1,4-NDC), Ce/Zr-UiO-66(1,4-NDC), and Ce/Ti-UiO-66(BDC-NH_2). (**a**) DR/UV-Vis between 200 and 800 nm, (**b**) band gap by Tauc plot analysis and baseline correction, (**c**) Tauc plot after correction, (**d**) PL spectroscopy, and (**e**) FT-IR spectra with regions related to key features indicated (M = Zr, Ce or Ti, see text).

2.4. Optical Properties

2.4.1. DR/UV-Vis Spectroscopy

DR/UV-Vis spectroscopy was used to determine the photo-response of the materials over wavelengths between 200 and 800 nm. As can be seen in Figure 4a, Ce/Ti-UiO-66(BDC-NH_2) showed a photo-response over a wide region of light, which implies that this sample had a narrow bandgap. As shown in Figure 4a, Ce/Zr-UiO-66(1,4-NDC/2,6-NDC), Ce/Zr-UiO-66(1,4-NDC) and Ce/Ti-UiO-66(1,4-NDC) had relatively similar levels of light absorption, compared to Ce/Ti-UiO-66(BDC-NH_2) and Ce/Zr-UiO-66(1,4-NDC/BDC), which showed different spectra. The only difference for Ce/Ti-UiO-66(-BDCNH_2) is related to the use of an electron-donating group (NH_2) in the linker, which increased E_{abs} and led to a bathochromic shift to above 350 nm [5,29]. The UV region between 200 and 350 nm indicates that Ce and Ti hexa-oxo clusters have good coordination with the linkers, thus enhancing the E_{LMCT} [30]. The E_{LMCT} from ligands transfers to the metal via 2p orbitals of carboxylate groups connected to 4f empty orbitals of Ce(IV) and 3d of Ti(IV) via μ-O_3, and causes a flat plateau over the wavelength between 200 and 400 nm [31]. As shown in Figure 3a, the intensity and the plateau of the spectra in most samples reveal that the negative value of the E_{LMCT} received by metal(s) plays a significant role in suppressing the recombination of photogenerated electrons between ground and excited states [31].

2.4.2. Estimating the Band Gap from the Tauc Plot

The Tauc method is suitable only for analyzing the spectra of pure semiconductors. When it is impossible to separate the spectrum into its components, a more precise estimation can be obtained using a baseline method [31]. As shown in Figure 4b, similar outcomes can be observed in the synthesized materials. The band gap increases in the order Ce/Ti-UiO-66(1,4-NDC) (1.86 $\pm$ 0.017 eV), Ce/Zr-UiO-66(1,4-NDC) (2.00 $\pm$ 0.018 eV), Ce/Zr-UiO-66(1,4-NDC/2,6-NDC) (2.08 $\pm$ 0.014 eV), Ce/Ti-UiO-66(BDC-NH_2) (2.41 $\pm$ 0.02 eV) and Ce/Zr-UiO-66(1,4-NDC/BDC) (2.69 $\pm$ 0.031 eV); see Figure 4c. The reported band gap of Zr-UiO-66 is between 3.5 and 4.10 eV, which is not useful for photocatalysis [32]. Extensive attempts have been devoted to tuning the band gap in UiO-66, and Yasin et al. reported that adding Ti into the Zr-UiO-66 structure reduces the band gap to 2.77 eV [33]. The band gaps of Ce/Ti-UiO-66(BDC-H/BDC-NH_2) and Ce-UiO-66(BDC-H/BDC-NH_2) have been reported as 2.84 and 1.92 eV, respectively, by Hou et al. for samples formed by a post-synthesis method [9,34]. Using rapid precipitation in this study reduced the band

gap of Ce-based UiO-66 to as low as 1.86 eV in Ce/Ti-UiO-66(1,4-NDC). Tuning UiO-66 via the use of hetero-metals and mixtures of organic linkers in this study and other reports reduced the band gap and increased the photocatalytic activities (see below).

Based on recent studies, missing linkers in UiO-66 play a significant role in decreasing the band gap, as well as increasing the E_{LMCT} and moving the E_{abs} to the visible light region [35]. The ideal UiO-66 ($[Zr_6O_4(OH)_4(BDC)_6]$) is highly coordinated with 12-fold connected linkers [36,37], and the mismatch of metals and the size of linkers can change the number of defects, reduce the band gap, and introduce photocatalytic activity, compared to non-defective UiO-66 [35]. As shown in Figure 4b, the band gap of Ce/Zr-UiO-66(1,4-NDC/BDC) is obviously larger than those of the other samples studied here, with a value of 2.69 eV. Missing linkers are seen in many samples; however, Ce/Ti combinations have the largest number in this series, with the number of missing linkers per cluster between 1.49 and 1.67—see Table 1. The literature shows that the number of defects per cluster can be between 0.1 and 3, and the modulator and solvent can be bonded to defective sites and balance the charge deficiencies [4,38,39]. A systematic study showed the use of benzoic acid to produce a different number of missing linkers per cluster—between 0.87 and 1.68 [39].

2.4.3. PL Spectroscopy

The recombination of photogenerated electrons in excited states was measured by PL spectroscopy to understand the nature of photocatalytic enhancement (see below). As can be seen in Figure 4d, the recombination of holes and electrons was extremely small for Ce/Zr-UiO-66(1,4-NDC), Ce/Ti-UiO-66(1,4-NDC) and Ce/Ti-UiO-66(BDC-NH_2), and for Ce/Zr-UiO-66(1,4-NDC/2,6-NDC) it was negligible. The suppression of the recombination of photogenerated carriers may be due to the narrower band gap, and oxygen vacancies in oxo-clusters may also contribute [40]. The results for Ce/Zr-UiO-66(1,4-NDC/BDC) show it achieved the highest values of electron–hole recombination in this series, which may be due to its non-defective structure. The results shown in Table 1 and Figure 4a–e provide good evidence that the defective structures achieved the maximum absorption of photons.

2.5. FT-IR Spectroscopy

FT-IR was used to investigate the nature of functional groups in the materials—see Figure 4e. The region between 400 and 700 cm^{-1} contains various bands involving metal–oxygen vibrations, and in the parent UiO-66(Zr), Zr-μ_3-O, Zr-OC and Zr-μ_3-OH vibrational modes have been assigned previously [41]. Other reports have noted shifts in these bands upon the inclusion of Ti [42] or Ce [43]; however, this region is difficult to assign, as the bands also become broadened upon metal substitution, and it is possible that this depends on the distribution of the metals within the clusters. The coordinated carboxylate shows bands at ~1580 cm^{-1} (asymmetric, ν_{as}(COO)) and 1440–1420 cm^{-1} (symmetric, ν_s(COO)) [38,44]. All the materials except Ce/Ti-UiO-66(BDC-NH_2) and Ce/Zr-UiO-66(1,4-NDC/BDC) showed a ν(C=O) band, which can be identified as a residual DMF solvent. The bending and stretching bands of amino functional groups are located at 1576 and 3346 cm^{-1}, respectively, and bending and stretching peaks of C=O and C-O are observed at 1605 and 3453 cm^{-1}, respectively, which are attributed to carboxylate groups of BDC-NH_2. Based on the non-defective structure of Ce/Zr-UiO-66(1,4-NDC/BDC), as shown in Table 1, the IR spectra are consistent with carboxylate groups fully connected to metals clusters.

2.6. Surface Area

The surface area in these samples is obviously smaller than those in other reported MTV-MOFs with the UiO-66 structure because of the use of multiple metals, linkers, and rapid precipitation, which could lead to some amorphous components. A systematic study showed that adding a second metal to UiO-66 decreases the surface area from 801 to 317 m^2g^{-1}, similar to these materials [45]. Regarding the synthesis method, room temperature precipitation gives materials with a smaller surface area than those produced by solvothermal synthesis [21,26,46]. As shown in Table 1, the surface area of these materials

is between 136.47 and 303.61 m^2g^{-1}, and Ce/Zr-UiO-66(1,4-NDC/2,6-NDC) and Ce/Ti-UiO-66(1,4-NDC) have the highest and lowest values in this series. Ce/Ti bimetallic derivatives have the smallest surface area in this series—between 136.47 and 144.08 m^2g^{-1}. The use of solvent, time, and heat can produce a larger surface area for UiO-66, between 900 and 1400 m^2g^{-1}, but careful activation of the materials is necessary to realize the optimal surface area, and any defects may lower the value achieved. Although a larger surface area can enhance the adsorption and catalytic activities of MOFs, Zr-UiO-66(BDC) with a surface area between 900 and 1100 m^2g^{-1} has weaker photocatalytic activities, with a band gap between 3.5 and 4.2 eV [47,48]. Based on these results, a small surface area does not lead to significant changes in photocatalytic activities, which suggests that MOF crystallites have high surface reactivity. Regarding the results of TGA, PXRD, and nitrogen adsorption, Ce/Ti-UiO-66(1,4-NDC) and Ce/Ti-UiO-66(BDC-NH_2) have the highest volume of unit cell, the largest number of ligand defects, and the lowest surface area, as shown in Table 1.

2.7. Surface Analysis of Electronic Structure of MTV-MOFs

X-ray photoelectron spectroscopy was used to determine the chemical features of the surfaces of the samples. Analysis of the spectra shows that the molar ratio of Ce toward Zr is 1 to 1 in both Ce/Zr-UiO-66(1,4-NDC/2,6-NDC) and Ce/Zr-UiO-66(1,4-NDC), as consistent with XRF—see Table 1. As shown in Figure 5a–e, the electronic properties of Zr were not changed in Ce/Zr-UiO-66(1,4-NDC/BDC), which suggests that the presence of Ce may not be enough to alter the electronic properties of the crystal structure. However, the electronic properties of the Zr cluster were changed in Ce/Zr-UiO-66(1,4-NDC/2,6-NDC) and Ce/Zr-UiO-66(1,4-NDC).

The presence of high percentages of Ce(III) on the surfaces of all materials was likely due to the reduction in Ce(IV) by mother liquor (DMF and warm water) during the synthesis; see Table 2 [49,50]. The features in the Ti spectrum were shifted in Ce/Ti-UiO-66(BDC-NH_2), likely due to changes in the electronic properties of Ti, which remained unchanged in Ce/Ti-UiO-66(1,4-NDC). The amino group had a serious impact on the reduction of Ce(IV) into Ce(III) during the MOF formation, which may have caused some further changes in the electronic properties of Ti in Ce/Ti-UiO-66(BDC-NH_2) in comparison with Ce/Ti-UiO-66(1,4-NDC); see Table 2.

Post-synthesis modification has been used previously to form Ce-UiO-66 with BDC-NH_2 linkers, and XPS showed the ligand exchange did not modify the electronic properties [9]. The amounts of Ce(III) and Ti(III) are important because both metals can be oxidized to their +4 oxidation state under exposure to different light sources [24]. The presence of Ce(III) and Ti(III) enhanced the E_{LMCT} and shifted the E_{abs} to the visible light region. The O 1s spectral region shows the availability of oxygen vacancies (O_V) derived from the lattice oxygen (O_{latt}), which aids the internal transfer of electrons within the oxidized and reduced states to produce (•OH) and superoxide ($•O_2^-$) free radicals—see Figure 5b [40]. Based on previous studies, incorporating Ti into UiO-66(Zr, Ce) influences the degree of hole–electron recombination [24,51], compared to Ce/Ti-UiO-66(1,4-NDC) and Ce/Ti-UiO-66(BDC-NH_2). As shown in Figure S2a–i, the C 1s spectrum of Ce/Ti-UiO-66(BDC-NH_2) shows features at 285 (C–C/C–H), 286 (C–O), 287 (C=O), 288 (C=O–O) and 290 eV (carbonates)—see Figure S2a–e. The presence of C-N/NR_4^+ in the spectrum confirms that the amino group survived in Ce/Ti-UiO-66(BDC-NH_2) [52], consistent with the FT-IR results (Figure 5e and Figure S2e). The oxygen 1s spectrum of Ce/Zr-UiO-66(1,4-NDC/BDC) has a different shape compared to those of the other four MTV-MOFs—see Figure S2. The lattice oxygen (O_{latt}), adsorption (O_{ads}), and surface-active oxygen (O_{sur}) show signals that appear between 534.38 and 530.35 eV—see Figure S2f–j [40]. The intensity of lattice oxygen (O_{latt}) in the XPS spectra indicates the presence of O_V in the crystal structure, which allows the internal transfer of electrons between the valence and conduction bands in metals to produce (•OH) and superoxide ($•O_2^-$) radicals [40]. The generation of radicals has previously been detected experimentally for UiO-66 photocatalysts [53]. The surface adsorption is tuned by the amount of O_{sur}, which can dominate the photocatalytic

activities [54]. The signals of O_{latt} and O_{sur} have lower and higher intensities in Ce/Zr-UiO-66(1,4-NDC/BDC), respectively, which can impact surface adsorption compared to other samples. The N 1s signals appear between 399 and 402 eV, and have been assigned to the C–N of NH_2 functionality in Ce/Ti-UiO-66(BDC-NH_2)—Figure S2k.

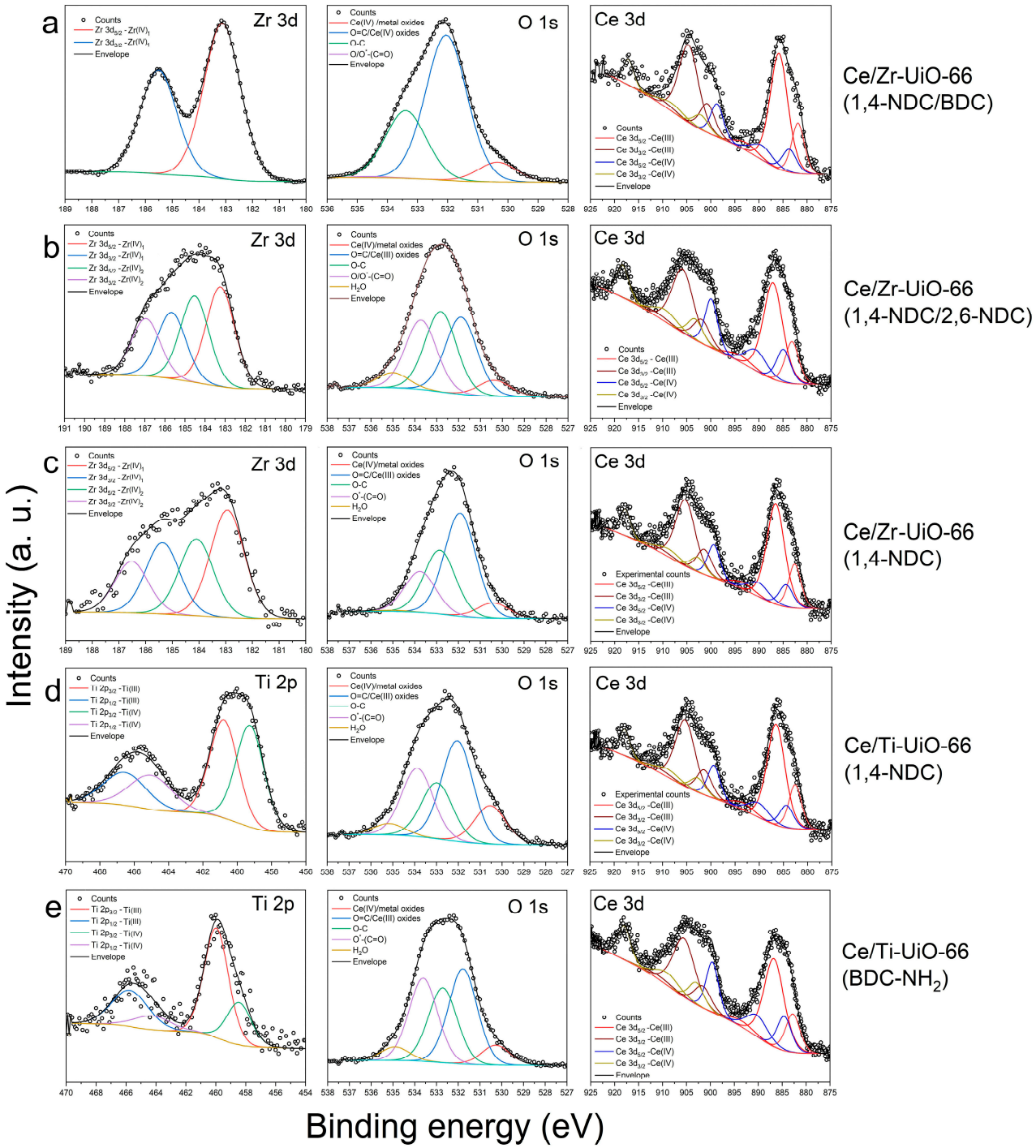

Figure 5. XPS spectra in the Ce 3d, Zr 3d, Ti 2p and O 1s regions for (**a**) Ce/Zr-UiO-66(1,4-NDC/BDC), (**b**) Ce/Zr-UiO-66(1,4-NDC/2,6-NDC), (**c**) Ce/Zr-UiO-66(1,4-NDC), (**d**) Ce/Ti-UiO-66(1,4-NDC) and (**e**) Ce/Ti-UiO-66(BDC-NH_2).

Table 2. XPS elemental compositions (%) of Ce 3d, Zr 3d, Ti 2p, Ce/Zr-UiO-66(1,4-NDC/BDC), Ce/Zr-UiO-66(1,4-NDC/2,6-NDC), Ce/Zr-UiO-66(1,4-NDC), Ce/Ti-UiO-66(1,4-NDC), and Ce/Ti-UiO-66(BDC-NH_2).

Sample	Elemental Composition and Oxidation State (Atomic %)									
	Ce	N	Zr	Ti	Ce(III)	Ce(IV)	Ce(III)/Ce(IV)	Ti(III)	Ti(IV)	Ti(III)/Ti(IV)
Ce/Zr-UiO-66(1,4-NDC/BDC)	1.3		1.8		65.3	34.7	1.9	-	-	-
Ce/Zr-UiO-66(1,4-NDC/2,6-NDC)	2.1	-	2.6	-	63.2	36.8	1.7	-	-	-
Ce/Zr-UiO-66(1,4-NDC)	2.1	-	2.3	-	71.4	28.6	2.5	-	-	-
Ce/Ti-UiO-66(1,4-NDC)	2.4	-	-	3.9	66.3	33.7	2.0	47.1	52.9	1.2
Ce/Ti-UiO-66(BDC-NH_2)	2.0	1.1	-	1.1	61.2	38.8	1.6	72	28	2.6

2.8. Adsorption

The photocatalytic degradation of dyes by MTV-MOFs was measured for two cationic and two anionic dyes at room temperature. In separate experiments, the photocatalytic degradation was measured in the dark, under UV and visible light irradiation. As can be seen in Figure 6a–d, Ce/Zr-UiO-66(1,4-NDC/BDC) showed a moderate level of photocatalytic activity towards anionic dyes (almost 50% degradation in 60 min); however, it showed the lowest photodegradation activity towards cationic dyes. Ce/Zr-UiO-66(1,4-NDC/BDC) showed an ability to adsorb anionic dyes. As shown in Figure 6c,d, adsorption increased for AR and CR compared to cationic dyes, which may be because the surface charge of Ce/Zr-UiO-66(1,4-NDC/BDC) is positive (+18 mV), as determined by zeta potential measurements—see Table 3. Previous systematic studies of the surface charge of UiO-66 shows that it can vary with pH between +40 (acidic solution) and -30 (basic solution) mV, and at pH 5, it is +18 mV [55], which is consistent with the surface charge of Ce/Zr-UiO-66(1,4-NDC/BDC), also measured at pH = 5. Both the value and positive surface charge play a significant role in surface adsorption in porous materials.

Ce/Zr-UiO-66(1,4-NDC/2,6-NDC) showed the greatest degree of adsorption towards cationic dyes—25 and 80 percent in 60 min for MB and RhB, respectively. The surface adsorption increased with anionic dyes to almost 100 percent in 60 min for CR, and a similar adsorption ability was seen for AR—see Figure S3a–d. Ce/Zr-UiO-66(1,4-NDC) showed a higher rate of adsorption for MB and CR and a lower rate for RhB and AR compared to Ce/Zr-UiO-66(1,4-NDC/2,6-NDC). Ce/Zr-UiO-66(1,4-NDC) absorbed 100 percent of MB in 50 min; however, it showed weak adsorption towards RhB, with 65 percent in 1 hour—see Figure 6e–h. The adsorption differences between MB and RhB may be because of the interaction between functional groups in methylene blue and the surface of Ce/Zr-UiO-66(1,4-NDC). The surface adsorption behaviors were similar for anionic dyes, with 100 and 30 percent adsorption in 60 min for CR and AR, respectively—see Figure S3e–h. Ce/Zr-UiO-66(1,4-NDC) weakly interacted with AR for dye adsorption and photocatalytic degradation. As shown in Figure S3i–l, Ce/Ti-UiO-66(1,4-NDC) achieved good surface adsorption towards methylene blue—60 percent in 1 hour. The sizes of pores in UiO-66 are not sufficient to trap the large dye molecules, and therefore dye adsorption is likely to take place on the surface [56].

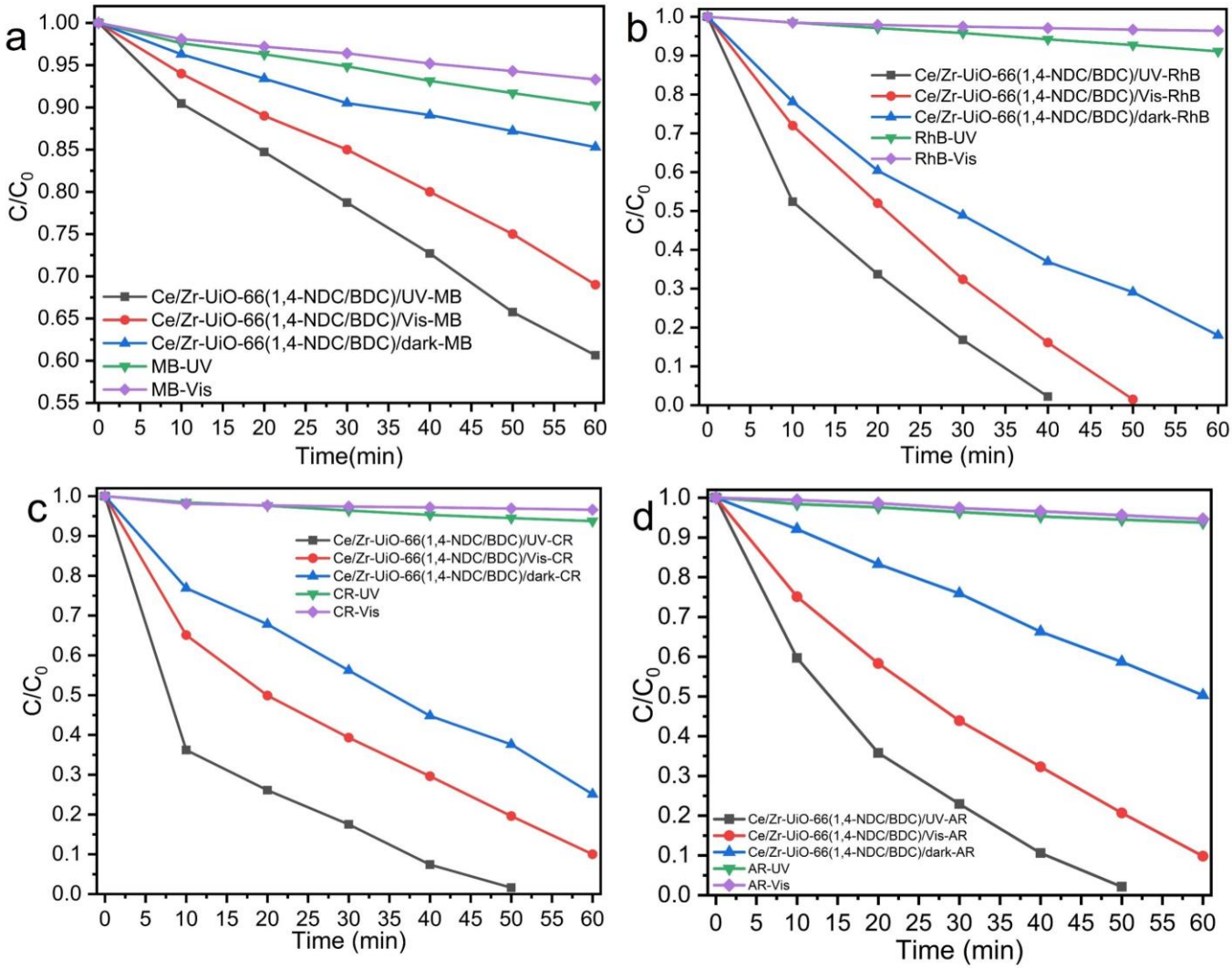

Figure 6. Photocatalytic activities of Ce/Zr-UiO-66(1,4-NDC/BDC) measured under UV and visible light in 60 min, towards (**a**) MB, (**b**) RhB, (**c**) CR, and (**d**) AR.

Table 3. Parameters for kinetic models of adsorption of cationic and anionic dyes by the UiO-66 series at 25 ppm.

		Pseudo-First Order			Pseudo-Second Order		
MOF	**Dye**	k_1 **(min^{-1})**	q_e **(mg·g^{-1})**	R^2	k_2 **(g·mg^{-1}min^{-1})**	q_e **(mg·g^{-1})**	R^2
Ce/Zr-UiO-66(1,4-NDC/BDC)	MB	5.6×10^{-2}	26.13	0.995	1.3×10^{-2}	33.11	0.998
Ce/Zr-UiO-66(1,4-NDC/2,6-NDC)	MB	5.2×10^{-2}	15.93	0.996	4.8×10^{-2}	38.31	0.998
Ce/Zr-UiO-66(1,4-NDC)	MB	6.0×10^{-2}	45.40	0.998	1.9×10^{-2}	15.22	0.991
Ce/Ti-UiO-66(1,4-NDC)	MB	6.2×10^{-2}	55.74	0.998	0.26	15.36	0.991
Ce/Ti-UiO-66(BDC-NH_2)	MB	6.2×10^{-2}	44.61	0.995	5.6×10^{-3}	17.06	0.991
Ce/Zr-UiO-66(1,4-NDC/BDC)	RhB	5.9×10^{-2}	72.31	0.994	4.3×10^{-3}	96.15	0.993
Ce/Zr-UiO-66(1,4-NDC-2,6-NDC)	RhB	2.3×10^{-2}	48.8	0.997	3.5×10^{-2}	26.95	0.995
Ce/Zr-UiO-66(1,4-NDC)	RhB	4.3×10^{-2}	110.91	0.998	2.6×10^{-3}	37.82	0.993
Ce/Ti-UiO-66(1,4-NDC)	RhB	5.0×10^{-2}	91.89	0.995	1.7×10^{-2}	10.52	0.996
Ce/Ti-UiO-66(BDC-NH_2)	RhB	6.1×10^{-2}	55.37	0.997	1.4×10^{-2}	30.211	0.995
Ce/Zr-UiO-66(1,4-NDC/BDC)	CR	4.9×10^{-2}	109.04	0.995	9.1×10^{-3}	31.25	0.991
Ce/Zr-UiO-66(1,4-NDC/2,6-NDC)	CR	2.8×10^{-2}	105.74	0.999	3.3×10^{-2}	14.28	0.986
Ce/Zr-UiO-66(1,4-NDC)	CR	5.4×10^{-2}	110.91	0.998	1.0×10^{-2}	29.69	0.990
Ce/Ti-UiO-66(1,4-NDC)	CR	7.5×10^{-2}	132.49	0.995	1.6×10^{-2}	16.28	0.984
Ce/Ti-UiO-66 (BDC-NH_2)	CR	4.9×10^{-2}	82.39	0.995	1.0×10^{-2}	30.41	0.990
Ce/Zr-UiO-66(1,4-NDC/BDC)	AR	2.4×10^{-2}	115.10	0.997	2.3×10^{-2}	22.75	0.961
Ce/Zr-UiO-66(1,4-NDC/2,6-NDC)	AR	6.4×10^{-2}	96.58	0.992	4.1×10^{-2}	11.89	0.986
Ce/Zr-UiO-66(1,4-NDC)	AR	5.3×10^{-2}	34.01	0.996	1.3×10^{-2}	60.20	0.998
Ce/Ti-UiO-66(1,4-NDC)	AR	4.1×10^{-2}	71.82	0.998	3.2×10^{-2}	76.05	0.998
Ce/Ti-UiO-66(BDC-NH_2)	AR	9.3×10^{-2}	67.27	0.990	3.8×10^{-2}	12.58	0.954

2.9. Kinetic Modeling of Adsorption

The rate and capacity of dye adsorption in the MTV-MOF series were investigated by the use of pseudo-first- and pseudo-second-order kinetic models—see Figures 7 and 8, and Table 3. As can be seen in Table 3, almost all followed the pseudo-first-order model due to higher values of R^2, compared to the pseudo-second-order model. The value of q_e for all MTV MOFs towards CR was, on average, greater than other dyes, which may be because all samples except Ce/Ti-UiO-66(1,4-NDC) had a positive surface charge—see Table 3. The values of q_e for the MTV-MOFs series towards CR are between 82.39 and 132.49 mg·g^{-1}, and those of k_1 are between 2.8 and 7.5 $\times$ 10^{-2} min^{-1}, which are favorable compared to other studies. Zhao et al. studied the capacity and rate of adsorption of various dyes by Ce-UiO-66 (with BDC as linker), and found an adsorption capacity of 168.5 mg·g^{-1} for RhB and 144.8 mg·g^{-1} for MB, which are rather higher than those of the samples of this study, and their rate constants calculated by the pseudo-first-order model were 0.1071 min^{-1} and 0.0879 min^{-1}, respectively [57]. Another study found the equilibrium adsorption capacity of MB by Ce-UiO-66 to be somewhat lower at 49 mg·g^{-1}, with a k_1 that was also lower, at

1.4×10^{-2} min^{-1}, while for CR, an equilibrium adsorption capacity of 123 $mg \cdot g^{-1}$ with $k_1 = 1.3 \times 10^{-2}$ min^{-1} was reported [57]. The observed values of equilibrium adsorption capacity in Ce/Ti-UiO-66(1,4-NDC) were the highest for UiO-66 derivatives. However, the reported values of equilibrium adsorption capacity for cationic dyes (MB and RhB) in other studies are higher than our results [58].

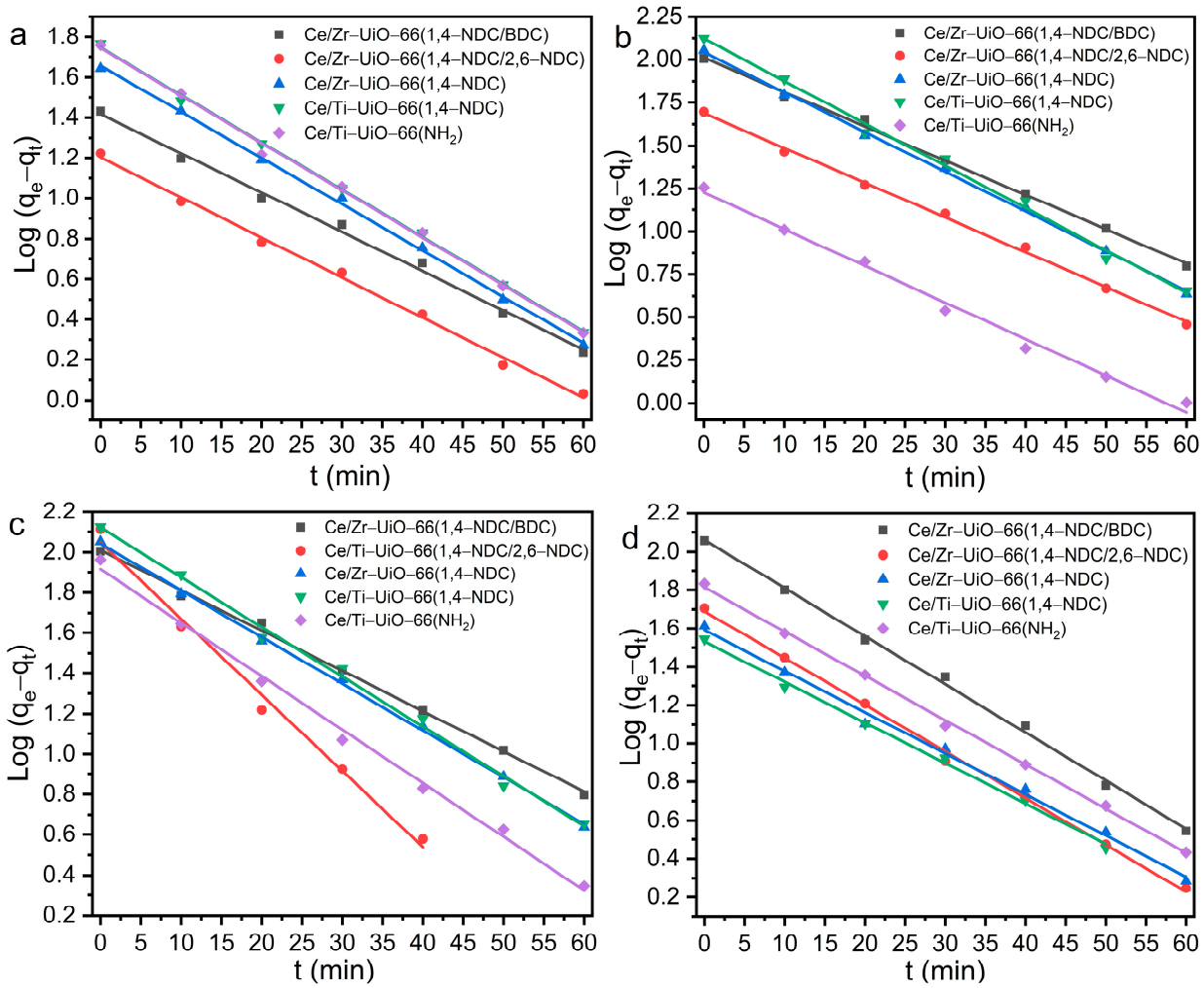

Figure 7. The pseudo-first-order kinetic model of dye degradation by Ce/Zr-UiO-66(1,4-NDC/BDC), Ce/Zr-UiO-66(1,4-NDC/2,6-NDC), Ce/Zr-UiO-66(1,4-NDC), Ce/Ti-UiO-66(1,4-NDC), and Ce/Ti-UiO-66(BDC-NH_2) for (**a**) MB, (**b**) RhB, (**c**) CR and (**d**) AR.

Based on other studies, the highest reported values of q_e for Ce-UiO-66 towards MB and RhB are 144.8 and 168.5 ($mg \cdot g^{-1}$), respectively, which are higher than those of the MTV-MOFs series studied here; however, the value of k_1 reported for Ce-UiO-66 is smaller than our finding [58]. The q_e values of Ce-UiO-66 (50 mg) towards CR and MB were reported as 123 and 49 ($mg \cdot g^{-1}$) [58], respectively, which are lower than those of Ce/Ti-UiO-66(1,4-NDC (30 mg)) towards the same dyes. In addition, the adsorption capacity of MB by Ce/Zr-UiO-66(1,4-NDC) was found to be 52.97 $mg \cdot g^{-1}$ in 30 mg/L of adsorbent.

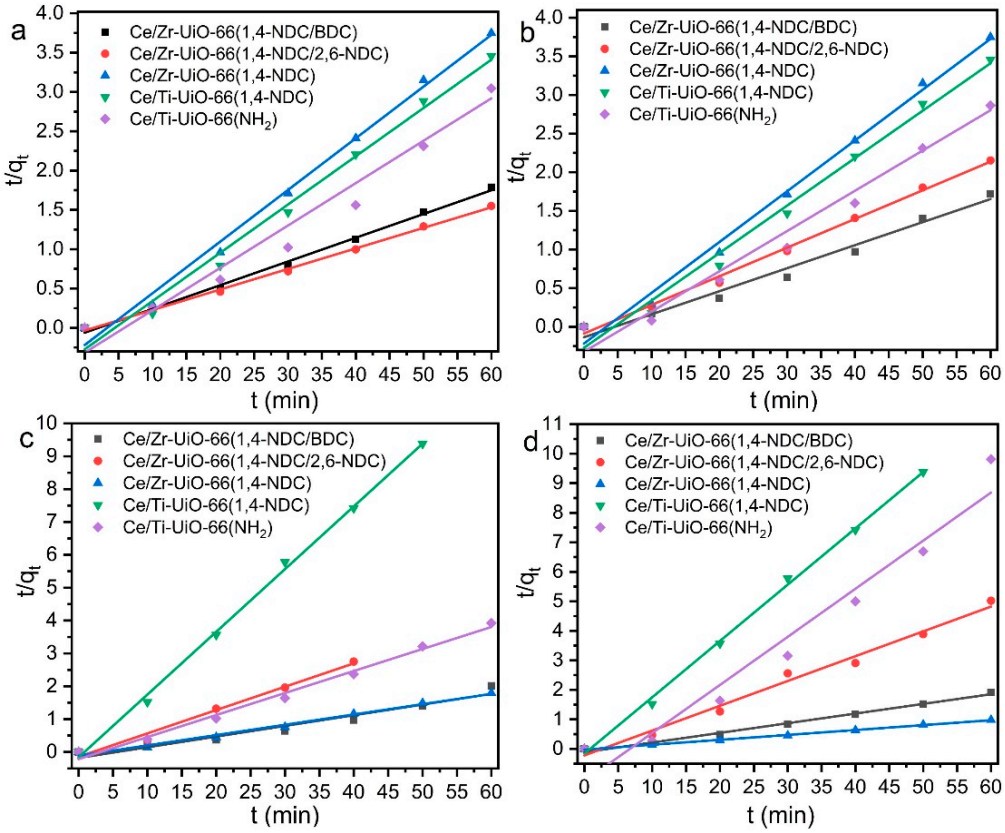

Figure 8. The pseudo-second-order kinetic model of dye degradation by UiO-66-X Ce/Zr-UiO-66(1,4-NDC/BDC), Ce/Zr-UiO-66(1,4-NDC/2,6-NDC), Ce/Zr-UiO-66(1,4-NDC), Ce/Ti-UiO-66(1,4-NDC), and Ce/Ti-UiO-66(BDC-NH_2) for (**a**) MB, (**b**) RhB, (**c**) CR and (**d**) AR.

As shown in Table 1 and Figure S4a–e, the surface areas of Ce/Zr-UiO-66(1,4-NDC/BDC), Ce/Zr-UiO-66(1,4-NDC/2,6-NDC), Ce/Zr-UiO-66(1,4-NDC), Ce/Ti-UiO-66(1,4-NDC), and Ce/Ti-UiO-66(BDC-NH_2) were 250.23, 303.61, 212.32, 136.47, and 144.08 m^2g^{-1}, respectively. The surface areas of the MTV-MOFs series synthesized by rapid precipitation were smaller than those of the MOFs produced by other methods, such as microwave or solvothermal [23,59]. The formation of a highly crystalline material requires an extended synthesis time; however, defective materials, such as those that contain missing linkers, may have larger surface areas [60]. The band gap in Ce/Ti-UiO-66(1,4-NDC) is greater than in Ce/Ti-UiO-66(BDC-NH_2), despite NH_2 being an electron-donating group, and it is unable to enhance the photocatalytic activities in UiO-66. In addition, the band gap of Ce/Zr-UiO-66 was found to be smaller than that of Ce/Ti-UiO-66(1,4-NDC); therefore, the use of different metals likely plays a significant role in controlling the photocatalytic activities. The surface area and surface charge of Ce/Zr-UiO-66(1,4-NDC/BDC) were 250.23 m^2g^{-1} and 18.33 mV, respectively. As shown in Table 1 and Figure 8, Ce/Zr-UiO-66(1,4-NDC/2,6-NDC) was defective with respect to missing linkers, and had the largest surface area among the MTV-MOF series, which led to a high capacity and rate of adsorption, especially towards anionic dyes; see Table 3. Ce/Ti-UiO-66(1,4-NDC) was the only sample with a negative surface charge and a higher adsorption capacity towards cationic dyes; however, it had the smallest surface area in this series.

2.10. Photocatalytic Activities

As shown in Figures 6c and 9a, Ce/Zr-UiO-66(1,4-NDC/BDC) gave the weakest photodegradation. It also has the highest value of band gap among the samples studied here, and the smallest number of missing ligands, which must play a significant role in its weakest performance, as shown in Table 1 and Figure 6a,b. Other samples exhibited

promising photocatalytic activity and could decolorize MB between 2 and 15 min under UV radiation, with Ce/Zr-UiO-66(1,4-NDC) having an exceptional capacity to bleach MB in only 2 min. The low electron and hole recombination and small band gap (1.84 eV) of Ce/Zr-UiO-66(1,4-NDC) may have been responsible for the photocatalytic activity. Ce/Ti-UiO-66(1,4-NDC) and Ce/Ti-UiO-66(BDC-NH_2) decolorized MB in 5 min and Ce/Zr-UiO-66(1,4-NDC/2,6-NDC) in 15 min. Based on visible light assessment, the trend of photodegradation performance is comparable to that of UV light (Figure 9a), and the process took relatively longer, between 10 and 25 min—see Figure 9b. RhB was decolorized by Ce/Zr-UiO-66(1,4-NDC/2,6-NDC) in 2 min, and by other samples in 7.5 to 12 min, which shows there were no significant changes between UV and visible light in this MTV-MOFs series—see Figure 9c. In contrast to MB decolorization, Ce/Zr-UiO-66(1,4-NDC/2,6-NDC) presented a very promising photocatalytic capacity to decolorize RhB in only 1 min, although the rest of the materials showed a strong photocatalytic degradation between 1.5 and 7.5 min—see Figure 9d. The explanation for the strong photocatalytic activities in Ce/Zr-UiO-66(1,4-NDC/2,6-NDC) is likely to be the maximum value of electron and hole suppression, defective structures, the use of 2,6-NDC as a photoluminescence linker, and the narrow band gap of 2.10 eV—see Figure 7b and Table 1. Based on the previous studies of the photocatalytic activities of MOFs, the time required for RhB decolorization is typically between 10 min and a few hours [61]. The samples studied here showed an exceptional performance in the degradation of cationic dyes; however, they showed different behaviors towards anionic dyes, except Ce/Zr-UiO-66(1,4-NDC/BDC). Ce/Ti-UiO-66(BDC-NH_2) achieved good photodegradation under UV and visible light irradiation, decolorizing CR in 3 and 7.5 min, respectively, due it possessing the largest band gap of this series as well as a defective structure. However, other samples showed weaker photocatalytic activities, with results between 7.5 and 50 min under UV, and between 20 and 60 min under visible light—see Figure 9e,f. Ce/Ti-UiO-66(1,4-NDC) achieved a promising photocatalytic activity, and it bleached AR in 7.5 and 30 min under UV and visible light emission, respectively. Ce/Zr-UiO-66(1,4-NDC) did not make any progress in 60 min under the two sources of light. Ce/Zr-UiO-66(1,4-NDC/2,6-NDC) and Ce/Ti-UiO-66(BDC-NH_2) achieved similar activities under different light sources—see Figure 9g,h. It seems Ti can increase photocatalytic activity and surface adsorption. In contrast, Ce/Ti-UiO-66(BDC-NH_2) showed weak dye adsorption; however, it presented strong photocatalytic activities towards both cationic and anionic dyes under both UV and visible light irradiation. Additionally, the electron-donating functional groups on the linkers decreased the E_{abs}, increased the E_{LMCT}, and transferred to the clusters, thus enhancing the photocatalytic activity—see Figure S3m–p.

To the best of our knowledge, Ce-NNU-15 achieved the fastest reported rate of decolorization of RhB, with 95 percent after 12 min [61]; however, Ce/Zr-UiO-66(1,4-NDC/2,6-NDC) took only a minute to decolorize RhB completely. TiO_2/GO (graphene oxide) is one of the most effective photocatalysts, and can decolorize 90 percent of MB in 20 min under UV [62], compared to the samples reported herein, which can bleach 100 percent of MB between 2 and 15 min. Hierarchical CuS–$Bi_2Cu_xW_{1-x}O_{6-2x}$ nanocomposite materials have been used to decolorize CR under visible light irradiation in 60 min [63]. In contrast, all samples in this study showed a strong ability to decolorize CR between 7.5 and 25 min under UV irradiation, with Ce/Ti-UiO-66(BDC-NH_2) having the shortest (7.5 min) and Ce/Zr-UiO-66(1,4-NDC/2,6-NDC) having the longest (25 min) decolorisation time. Another study showed that doping Bi^{3+} in TiO_2 nanoparticles increases the photocatalytic capacity, enabling them to decolorize 80 percent of AR in 60 min under visible light emission [64]; however, all the MTV-MOFs reported here could bleach 100 percent of AR between 30 and 40 min.

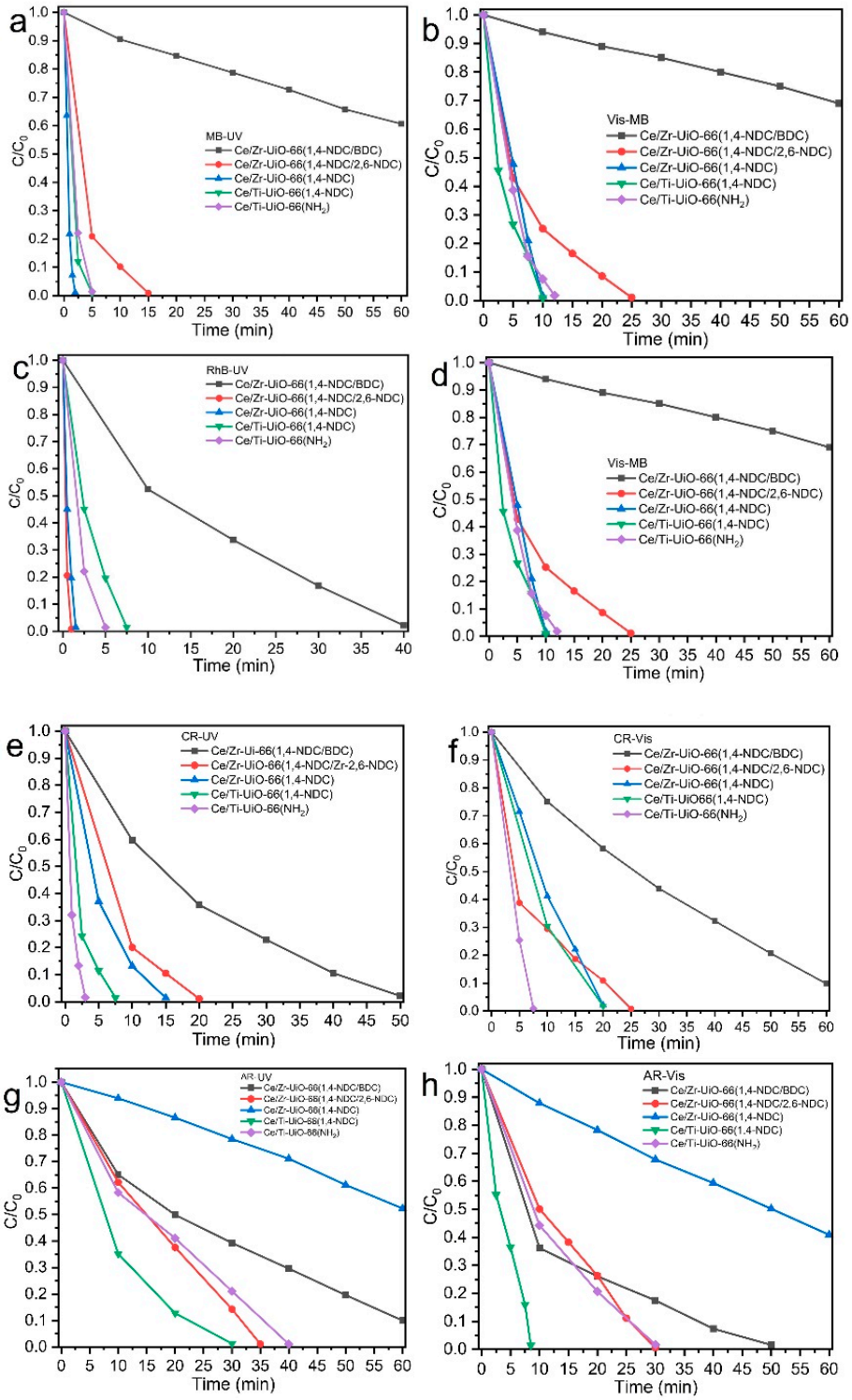

Figure 9. Photocatalytic dye measurements of MTV-MOF series (Ce/Zr-UiO-66(1,4-NDC/2,6-NDC), Ce/Zr-UiO-66(1,4-NDC), Ce/Ti-UiO-66(BDC-NH_2), and Ce/Ti-UiO-66(1,4-NDC)) in cationic (MB, RhB) and anionic (CR, AR) dye solutions under UV and visible light, (**a**) MB-Vis, (**b**) MB-UV, (**c**) RhB-Vis, (**d**) RhB-UV, (**e**) CR-Vis, (**f**) CR-UV, (**g**) AR-Vis, and (**h**) AR-UV.

2.11. Recyclability

Based on the good photocatalytic performances of Ce/Zr-UiO-66(1,4-NDC/2,6-NDC), Ce/Zr-UiO-66(1,4-NDC), Ce/Ti-UiO-66(1,4-NDC), and Ce/Ti-UiO-66(BDC-NH_2), the measurements of photo-stability and recyclability were determined over 17 h and five cycles,

respectively, as shown in Figure 10a–h. All samples were stable under UV exposure for 17 h. PXRD confirmed the structural stability, showing that the structures were retained after decolorization; see Figure S5a–d. However, the intensity of Bragg peaks was reduced. Ce/Zr-UiO-66(1,4-NDC) showed promising recyclability under UV and visible light irradiation, and the samples remained unchanged after each cycle compared to other materials—see Figure 10b.

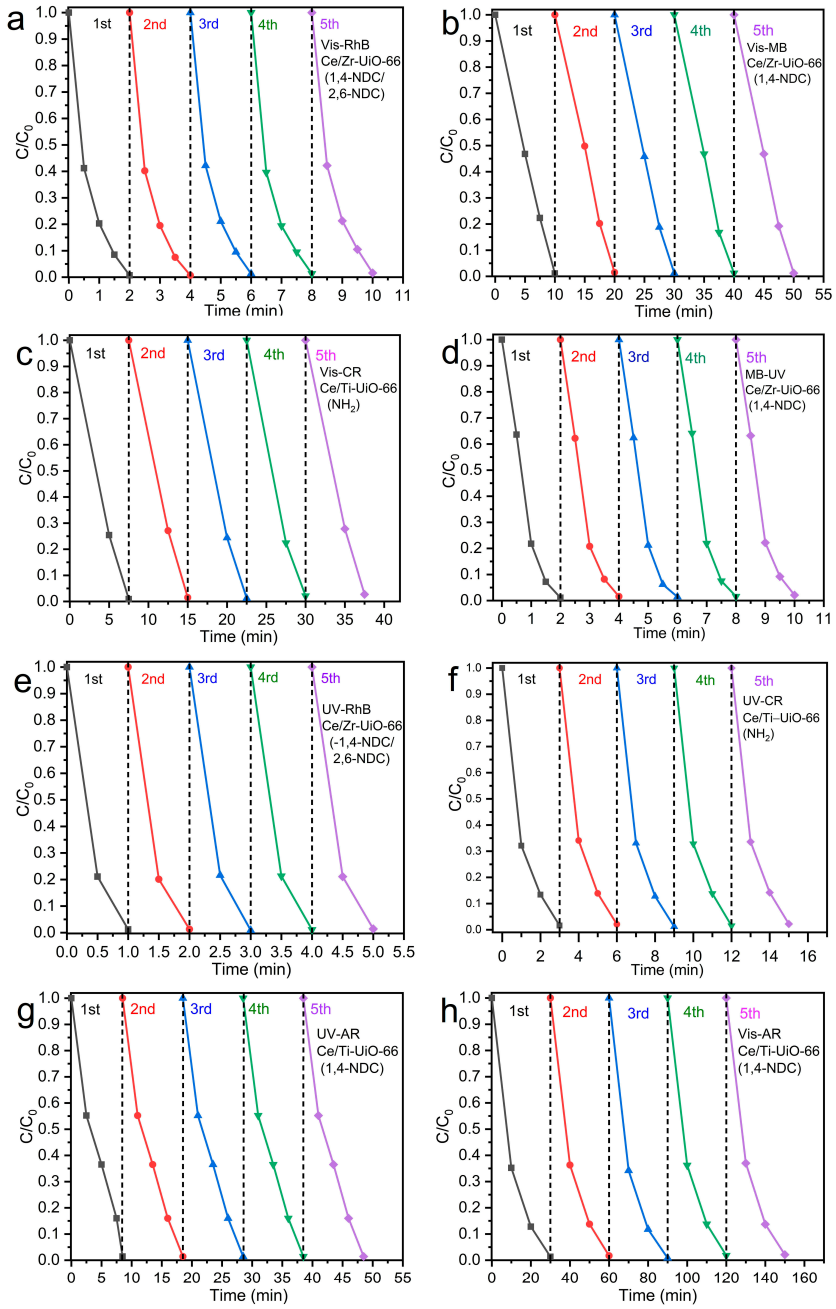

Figure 10. Five runs of recyclability of MTV-MOFs at room temperature (**a**) Ce/Zr-UiO-66(1,4-NDC/2,6-NDC) in RhB under visible light, (**b**) Ce/Zr-UiO-66(1,4-NDC) in MB under visible light, (**c**) Ce/Ti-UiO-66(BDC-NH_2) in CR under visible light, (**d**) C/Zr-UiO-66(1,4-NDC) in MB under UV light, (**e**) Ce/Zr-UiO-66(1,4-NDC/2,6-NDC) in RhB under UV light, (**f**) Ce/Ti-UiO-66(1,4-NDC) in CR under UV light, (**g**) Ce/Ti-UiO-66(1,4-NDC) in AR under UV light and (**h**) Ce/Ti-UiO-66(1,4-NDC) in AR under visible light.

3. Materials and Methods

3.1. Sample Preparation

3.1.1. Materials

Chemical reagents: ammonium cerium nitrate ($(NH_4)_2Ce(NO_3)_6$, Merck); titanium(IV) isopropoxide (Sigma-Aldrich, Gillingham, UK) 97%; zirconium(IV) chloride ($ZrCl_4$, Sigma-Aldrich, Gillingham, UK) 99.5%; benzene-1,4-dicarboxylic acid and 2-amino benzene-1,4-dicarboxylic acid (Fisher Scientific, Loughborough, UK) 99%; naphthalene-1,4-dicarboxylic acid (Sigma-Aldrich, Gillingham, UK) 94%; naphthalene-2,6-dicarboxylic acid (Sigma Aldrich, Gillingham, UK) 99%; potassium hydroxide (Sigma-Aldrich, Gillingham, UK) 90% were used as provided.

Solvents: DMF (*N*,*N*-dimethylformamide, Scientific Laboratory Supplies Ltd, West Bridgford, UK) 99.8%; triethylamine (Sigma-Aldrich, Gillingham, UK) 99.5%; acetic acid (Merck) 100%; ammonium fluoride (Sigma-Aldrich, Gillingham, UK) 99% and deuterium oxide (Sigma-Aldrich, Gillingham, UK) 99.9% were used as supplied. A Simplicity UV ultrapure water purification system (Merck Millipore, Burlington, Massachusetts, USA) was used to produce deionized water (18 MΩ cm).

3.1.2. Preparation of MTV-MOFs

Ce/Zr-UiO-66(1,4-NDC/BDC)

$ZrCl_4$ (0.116 g, 0.5 mmol) and 1,4-H_2NDC (0.108 g, 0.5 mmol) were dissolved in 15 mL DMF, and H_2BDC (83 mg, 0.5 mmol) was added to the solution and sonicated in an ultrasound bath (240 W) to obtain a transparent solution. Then, 5 mL of acetic acid was added into 10 mL of warm water (52 °C). $Ce(NH_4)_2(NO_3)_6$ (0.15 g) was dissolved in 2 mL of water separately (23 °C). Then, these two solutions were added to each other. An orange precipitate appeared rapidly. The solid sample was washed three times with acetone. The pristine sample was collected by centrifugation, washed 3 times with acetone (4000 rpm for 3 min), and dried at 100 °C, and the yield was 95%.

Ce/Zr-UiO-66(1,4-NDC/2,6-NDC)

$(NH_4)_2Ce(NO_3)_6$ (0.269 g, 0.5 mmol) and $ZrCl_4$ (0.116 g, 0.5 mmol) were dissolved in 2 mL of water (23 °C), using an ultrasonic bath (240 W) to make a transparent solution. 2,6-H_2NDC (0.108 g, 0.5 mmol) was dissolved separately in 15 mL DMF using an ultrasound bath (240 W) for 5 min to obtain a clear solution and 1,4-H_2NDC (0.108 g, 0.5 mmol) was added to the solution and sonicated for 2 more minutes. Then, 2.5 mL acetic acid and 9 drops of KOH (10 M) were added to 15 mL of water (60 °C). Then, the solutions of metal and of linker were added to the acetic acid/KOH solution. A yellowish precipitate immediately appeared. The pH of the solution was 5 and the temperature of the mixture was 50 °C. The sample was collected by centrifugation, washed 3 times with acetone (4000 rpm for 3 min for each), and dried at 110 °C. The yield was 56%. To remove unreacted precursors from the as-synthesized MOF, the sample was stirred in 15 mL water for 20 min at room temperature, and the yield was 91%.

Ce/Zr-UiO-66(1,4-NDC)

$(NH_4)_2Ce(NO_3)_6$ (0.269 g, 0.5 mmol) and $ZrCl_4$ (0.116 g, 0.5 mmol) were dissolved in 2 mL water (23 °C). 1,4-H_2NDC (0.216 g, 1 mmol) was dissolved separately in 15 mL DMF using an ultrasound bath (240 W) to obtain transparent solutions. The, 5 mL acetic acid was added to 5 mL water (59 °C). Then the solutions of metal and of linker were added to the warm acetic acid aqueous solution. A yellowish precipitate immediately appeared, and the pH and temperature of the solution were 5 and 48 °C, respectively. The pristine sample was collected by centrifugation, washed 3 times with acetone (4000 rpm for 3 min each time), and dried at 110 °C, giving a yield of 81%.

Ce/Ti-UiO-66(1,4-NDC)

$Ce(NH_4)_2(NO_3)_6$ (0.269 g, 0.5 mmol) was dissolved in 1.5 mL water (23 °C) and 1,4-H_2NDC (0.216.19 g, 1 mmol) was dissolved in 7 mL DMF. Then, 0.1 mL of titanium(IV)

isopropoxide (0.505 mg, 11 mmol) was added to the solution and dispersed using an ultrasound bath (240 W) for 10 min. Then, 3 mL acetic acid and 1 mL KOH (10 M) were added to 15 mL of water at 60 °C. Then, the first two solutions (metals and linker) were added to the warm solution of acetic acid/KOH, leading to an orange precipitate. The pH and temperature of solution were 5 and 49 °C, respectively. The pristine sample was collected by centrifugation, washed 3 times with acetone (4000 rpm for 3 min for each), and dried at 110 °C. The yield was 85%.

Ce/Ti-UiO-66(BDC-NH_2)

$Ce(NH_4)_2(NO_3)_6$ (0.269 g, 0.5 mmol) was dissolved in 1.5 mL of water (23 °C) and H_2BDC-NH_2 (0.188 g, 1 mmol) was dissolved in 7.5 mL DMF. Then, 0.2 mL of titanium(IV) isopropoxide (0.221 mg, 4.2 mmol) was added to the solution and dispersed using an ultrasound bath (240 W) for 10 min. Then, 3 mL of acetic acid and 1 mL KOH (10 M) were added to 15 mL of water at 60 °C. Then, two solutions (metals and linker) were added to the third solution. A brown precipitate immediately appeared, and the pH and temperature of the solution were 5 and 50 °C, respectively. The pristine sample was collected by centrifugation, washed 3 times with acetone (4000 rpm for 3 min each), and dried at 110 °C. The yield was 75%.

3.2. Experimental Methods

3.2.1. Characterization and Analysis

Powder X-ray diffraction (PXRD) measurements were conducted on a Panalytical Empyrean (Malvern Panalytical, Malvern, UK) diffractometer, using copper $K\alpha_{1/2}$ radiation with a mean wavelength of 1.5418 Å. Data were collected between 5 and 50° 2θ. The powdered material was compacted onto a flat silicon holder. GSAS-II software (version 4760) was employed for profile fitting of the PXRD patterns, to ascertain unit cell metrics [65]. Fourier transform infrared spectroscopy (FT-IR) on a Bruker ALPHA Platinum ATR device (Bruker (UK) Ltd., Coventry, UK) was used to detect specific organic functional groups. Each reading involved 8 combined scans within a 4000–600 cm^{-1} range. Thermogravimetric analysis (TGA) was performed on a Mettler Toledo STAR^e system (Leicester, UK) from 26 to 1000 °C in an air atmosphere at a 50 mL/minute flow. Samples of about 10 mg were placed in a ceramic crucible. Scanning electron microscopy (SEM) was executed on a Zeiss Gemini (Karl Zeiss, Oberkochen, Germany), operating at 3 kV and a resolution of 1 nm at 1 kV and 0.6 nm. UV-Vis diffuse reflectance spectroscopy (DRS) was recorded using a Shimadzu UV-2600 device (Kyoto, Japan), with $BaSO_4$ as the standard. These UV-Vis readings were taken at ambient temperature, spanning 200–800 nm at a rate of 200 nm/min. X-ray photoelectron spectroscopy (XPS) was used to identify the surface metal oxidation states and band gaps of the samples using a Kratos AXIS Ultra DLD (Manchester, UK) in a UHV system with a base pressure below 1×10^{-10} mbar. The sample was excited with X-rays from a monochromated Al K a source (1486.7 eV), with the photoelectrons being detected at a 90° take-off angle with respect to the sample surface. Curve fitting analysis was conducted with the CasaXPS software (version 2.3.25), using Voigt (a combination of Gaussian and Lorentzian) line profiles and Shirley baselines for every region [66].

Photoluminescence (PL) spectroscopy measurements were taken with a Renishaw Via Reflex Raman Microscope (Wotton-under-Edge, UK) to establish an excitation wavelength at 325 nm operating at 0.1% intensity, roughly 0.006 mW. Each assessment took 10 s across two scans. Nitrogen (N_2) adsorption studies were conducted on a Micromeritics ASAP2020 (Tewkesbury, UK) gas absorption device. Every sample was degassed in the range of 150 to 200 °C for 12 h, depending on its stability, to eliminate any residual solvents within the cavities. The surface area calculation was performed at 77 K over 7 h, based on the variations in relative pressure as per the Brunauer–Emmett–Teller (BET) methodology. Zeta potential measurements were carried out using an Anton–Paar Litesizer 500 and Omega cuvettes (Graz, Austria). Experiments were performed at a consistent 25 °C following a 5 s temperature stabilization phase.

^{1}H NMR spectra were measured using a Bruker AVIII HD-300 MHz spectrometer (Coventry, UK). D_2O and ammonium fluoride were used to digest MOFs before running an analysis to determine the relative amounts of mixed linkers. D_2O was used as the NMR reference solvent throughout the measurement, and the scan duration was 3 min. For the analysis of all the ^{1}H NMR spectra described, the TopSpin software (version 4, Bruker Corporation, Coventry, UK) was used.

3.2.2. Photodegradation Studies

MOFs were evaluated by examining the degradation of two cationic dyes (methylene blue and rhodamine B) and two anionic dyes (Congo red and Alizarin red s (AR)) under both UV and visible light at ambient temperature. A 6 watt handheld UV lamp (UVGL-55, Analytik Jena AG, Jena, Germany) with a 254 nm wavelength was used for UV light tests, while a 400 W portable halogen light (SFD limited BA22-Arundel UK) served as the visible light source. For every trial, 35 mg of MOF was mixed in 150 mL solutions of varying concentrations of the dyes. The photocatalysts were first dispersed using an ultrasonic bath for a minute, with Ce/Ti-UiO-66(BDC-NH_2) subjected to an additional 3 min to prevent particle agglomeration.

During the photocatalytic test, MOFs and dye solutions were continuously mixed using a magnetic stirrer to ensure uniformity. UV and visible light analyses typically spanned 10 min, but the interval was occasionally shortened to 20 s to capture rapid degradation shifts. To remove MOF particles, the solution underwent centrifugation for 5 min at 13,100 rpm. Residual solution absorbance changes during degradation were recorded with a Perkin Elmer Lambda XLS/XLS+ (Waltham, MA, USA) using the formula:

$$A = \frac{C_0 - C_t}{C_0} \times 100 \quad (1)$$

where C_0 and C_t are the initial concentration and the concentration at time t, respectively [67].

Adsorption tests took place in darkness, mirroring the photocatalytic evaluations under light conditions. To determine adsorption rates and capacities between the dyes and UiO-66 in darkness, pseudo-first- and pseudo-second-order kinetic models were employed [68].

The adsorption capacities (q_e and q_t) of the UiO-66 series in dye solutions were estimated using the following equations.

Adsorption capacity (q_e) at equilibrium concentration:

$$q_e = \frac{(C_0 - C_e)V}{m} \quad (2)$$

Adsorption capacity at time (q_t):

$$q_t = \frac{(C_0 - C_t)V}{m} \quad (3)$$

C_0 is the initial concentration at time of start (t = 0), and C_t is concentration at reaction time (t). C_e, m, and V are equilibrium concentration, the mass of adsorbent (in g), and the volume of solution (in L), respectively.

The pseudo-first-order used took the form:

$$log\ (q_e - q_t) = log\ q_e \frac{k_1}{2.303} t \quad (4)$$

q_e and q_t are the amount of dye adsorbed at equilibrium and at time t, respectively, and (mg/g) and k_1 (min^{-1}) are the rate constant. The value of k_1 was determined from plots of log ($q_e - q_t$) versus t.

The pseudo-second-order took the form:

$$\frac{t}{q_t} = \frac{1}{k_2 q_e^2} + \frac{t}{q_e} \quad (5)$$

k_2 (g·mg^{-1}min^{-1}) is the rate constant for adsorption. A plot of t/q_t versus t gives the values of q_e and k_2.

4. Conclusions

This study used the precipitation method to synthesize MTV-MOFs with a UiO-66 structure with mixtures of metals and mixtures of linkers to modify the photocatalytic properties of the materials. The adsorption of dyes by MTV-MOFs followed the pseudo-first-order kinetic model and showed good adsorption capacities. All samples showed a promising photocatalytic activity, photostability, and recyclability. The incorporation of a second metal in the MOF structure can enhance the photocatalytic activities, which can be furthered by using electron-donating groups on the organic linkers, while the defective structures showed a good photocatalytic activity, compared to non-defective structures. Using multiple reactive metals (Ce and Ti) and electron-donating linkers (BDC-NH_2), the electronic properties can be tailored to suppress the recombination of photogenerated electrons among the excited states, reduce the band gap, and prolong the photogenerated electrons. Rapid precipitation directly forms UiO-66 with Ce, Ti, and BDC-NH_2—to our knowledge, this is the first time that this combination of metals and linkers has been reported. The lowest band gap in the MTV-MOFs reported is 1.86 eV for Ce/Ti-UiO-66(1,4-NDC), which also had the lowest hole–electron recombination and the highest rate of photocatalytic activity. Other samples showed higher band gaps between 2.00 and 2.68 eV. Most samples can decolorize cationic and anionic dyes between 1 and 30 min under UV and visible light irradiation. In future work, it would be useful to investigate the mechanism of dye degradation to understand how the properties of the materials might be further optimized. The rapid precipitation suggests a scalable method of MTV-MOFs production for future work.

Supplementary Materials: The following supporting information can be downloaded at: https://www.mdpi.com/article/10.3390/inorganics11120455/s1. Figure S1: The thermogravimetric analysis (TGA) curves of MTV-MOFs series showing the continuous weight loss until ca. 500 °C, (a) Ce/Zr-UiO-66(1,4-NDC/BDC), (b) Ce/Zr-UiO-66(1,4-NDC/2,6-NDC), (c) Ce/Zr-UiO-66(1,4-NDC), (d) Ce/Ti-UiO-66(1,4-NDC), (e) Ce/Zr-UiO-66(NH_2). thermal decomposition step is labelled X_1 and X_2 which is first mass loss(solvent, modulator, and water), and total ligand combustion, respectively. M_1 and M_2 are the theoretical and actual masses of MTV-MOFs, respectively; Figure S2: XPS spectra of **C 1S**: (a) Ce/Zr-(1,4-NDC/BDC), (b) Ce/Zr-(1,4-NDC/2,6-NDC), (c) Ce/Zr-UiO-66(1,4-NDC), (d) Ce/Ti-UiO-66(1,4-NDC), and (e) Ce/Ti-UiO66(NH_2). **O 1s**: (f)Ce/Zr-(1,4-NDC/BDC), (g) Ce/Zr-(1,4-NDC/2,6-NDC), (h) Ce/Zr-UiO-66(1,4-NDC), (i) Ce/Ti-UiO(1,4-NDC), and (j) Ce/Ti-UiO66(NH_2), **N 1s**: (k) Ce/Ti-UiO66(NH_2);Figure S3: Photocatalytic activities, Ce/Zr-UiO-66(1,4-NDC/BDC), Ce/Zr-UiO-66(1,4-NDC/2,6-NDC), Ce/Zr-UiO-66(1,4-NDC), Ce/Ti-UiO-66(1,4-NDC), and Ce/Ti-UiO-66(NH_2) measured under UV, visible, and in MB, RhB, CR, and AR in 60 min; Figure S4: Nitrogen adsorption(black)–desorption(red) isotherms of MTV-MOFs, Ce/Zr-UiO-66(1,4-NDC/BDC), Ce/Zr-UiO-66(1,4-NDC/2,6-NDC), Ce/Zr-UiO-66(1,4-NDC), Ce/Ti-UiO-66(1,4-NDC), Ce/Ti-UiO-66(NH_2); Figure S5: PXRD after 5 cycles and 17 hours of UV stability of MTV-MOFs, (a) Ce/Zr-UiO-66-(1,4-NDC/2,6-NDC), (b) Ce/Zr-UiO-66(1,4-NDC), (c) Ce/Ti-UiO-66(1,4-NDC), (d) Ce/Ti-UiO-66(NH_2); Figure S6: 1H-NMR spectra obtained after digestion of Ce/Zr-UiO-66(1,4-NDC/BDC); Figure S7: 1H-NMR spectra obtained on the Ce/Zr-UiO-66(1,4-NDC/2,6-NDC); Table S1a: Details of the deconvolution and ranges of energies of the features in the XPS spectrum of Ce/Zr-UiO-66(1,4-NDC/BDC) including binding energy, the nature of bonding in samples, and their percentages; Table S1b: Details of the deconvolution and ranges of energies of the features in the XPS spectrum of Ce/Zr-UiO-66(1,4-NDC/2,6-NDC) including binding energy, the nature of bonding in samples, and their percentages; Table S1c: Details of the deconvolution and ranges of energies of the features in the XPS spectrum of Ce/Zr-UiO-66(1,4-NDC) including binding energy, the nature of

bonding in samples, and their percentages; Table S1d: Details of the deconvolution and ranges of energies of the features in the XPS spectrum of Ce/Ti-UiO-66(1,4-NDC) including binding energy, the nature of bonding in samples, and their percentages; Table S1e: Details of the deconvolution and ranges of energies of the features in the XPS spectrum of Ce/Ti-UiO-66(NH_2) including binding energy, the nature of bonding in samples, and their percentages; Table S2: The number of protons, value of peak integrals, and calculation of the molar ratio of linkers in Ce/Zr-UiO-66(1,4-NDC/BDC) and Ce/Zr-UiO-66(1,4-NDC/2,6-NDC).

Author Contributions: Conceptualization, E.E.G. and R.I.W.; methodology, E.E.G.; formal analysis, E.E.G. and M.W.; investigation E.E.G.; writing—original draft preparation, E.E.G.; writing—review and editing, E.E.G. and R.I.W.; supervision, R.I.W. All authors have read and agreed to the published version of the manuscript.

Funding: E.E.G. is grateful to the University of Warwick for the provision of a PhD scholarship and CARA for support. M.W. acknowledges financial support from the EPSRC-funded Warwick Analytical Science Centre (EP/V007688/1).

Data Availability Statement: The research data supporting this publication can be accessed at https://wrap.warwick.ac.uk/181255.

Acknowledgments: Some of the equipment used in this research was provided by the University of Warwick Research Technology Platforms, and we thank Rajan Randev, David Walker, Daniel Lester, Ben Breeze, Chris Waldron, Katie Pickering, Joseph Gregory and Garett Jackson for assistance with some of the measurements.

Conflicts of Interest: The authors declare no conflict of interest.

References

1. Zhe, J.; Tong, L.; Yaghi, O.M. Sequencing of Metals in Multivariate Metal-organic Frameworks. *Science* **2020**, *369*, 674–680.
2. Patial, S.; Raizada, P.; Hasija, V.P.; Thakur Singh, V.K.; Nguyen, V.H. Recent Advances in Photocatalytic Multivariate Metal-organic Frameworks-Based Nanostructures toward Renewable Energy and The Removal of Environmental Pollutants. *Mater. Today Energy* **2021**, *19*, 100589. [CrossRef]
3. Helal, A.; Yamani, Z.H.; Cordova, K.E.; Yaghi, O.M. Multivariate Metal-Organic Frameworks. *Natl. Sci. Rev.* **2017**, *4*, 296–298. [CrossRef]
4. Feng, X.; Hajek, J.; Jena, H.S.; Wang, G.; Veerapandian, S.K.P.; Morent, R.; De Geyter, N.; Leyssens, K.; Hoffman, A.E.J.; Meynen, V.; et al. Engineering a Highly Defective Stable UiO-66 with Tunable Lewis- Brønsted Acidity: The Role of the Hemilabile Linker. *J. Am. Chem. Soc.* **2020**, *142*, 3174–3183. [CrossRef]
5. Wu, X.P.; Gagliardi, L.; Truhlar, D.G.; Truhlar, D.G. Cerium Metal–organic Framework for Photocatalysis. *J. Am. Chem. Soc.* **2018**, *140*, 7904–7912. [CrossRef]
6. Schelter, E.J. Cerium under the Lens. *Nat. Chem.* **2013**, *5*, 348. [CrossRef]
7. Wu, X.P.; Gagliardi, L.; Truhlar, D.G.; Truhlar, D.G. Metal Doping in Cerium Metal-Organic Frameworks for Visible-Response Water Splitting Photocatalysts. *Chem. Phys.* **2018**, *150*, 041701. [CrossRef]
8. Santiago Portillo, A.; Baldoví, H.G.; García Fernandez, M.T.; Navalón, S.; Atienzar, P.; Ferrer, B.; Alvaro, M.; Garcia, H.; Li, Z. Ti as Mediator in the Photoinduced Electron Transfer of Mixed-Metal NH_2–UiO-66(Zr/Ti): Transient Absorption Spectroscopy Study and Application in Photovoltaic Cell. *J. Phys. Chem. C* **2017**, *121*, 7015–7024. [CrossRef]
9. Hou, W.; Chen, C.; Xie, D.; Xu, Y. Substituted Ti(IV) in Ce-UiO-66-NH_2 Metal–Organic Frameworks Increases H_2 and O_2 Evolution under Visible Light. *ACS Appl. Mater. Interfaces* **2023**, *15*, 2911–2921. [CrossRef]
10. Bůžek, D.; Demel, J.; Lang, K. Zirconium Metal–Organic Framework UiO-66: Stability in an Aqueous Environment and Its Relevance for Organophosphate Degradation. *Inorg. Chem.* **2018**, *57*, 14290–14297. [CrossRef]
11. Zhang, T.; Lin, W. Metal–Organic Frameworks for Artificial Photosynthesis and Photocatalysis. *Chem. Soc. Rev.* **2014**, *43*, 5982–5993. [CrossRef]
12. Gómez-Avilés, A.; Solís, R.R.; García-Frutos, E.M.; Bedia, J.; Belver, C. Novel Isoreticular UiO-66-NH_2 Frameworks by N-Cycloalkyl Functionalization of the 2-Aminoterephtalate Linker with Enhanced Solar Photocatalytic Degradation of Acetaminophen. *J. Chem. Eng.* **2023**, *461*, 141889-02. [CrossRef]
13. Yu, F.; Chen, L.; Shen, X.; Li, X.; Duan, C. NH_2-UiO-66/G-C_3N_4/CdTe Composites for Photocatalytic Reduction under Visible Light. *APL Mater.* **2019**, *7*, 101101. [CrossRef]
14. Chatenever, A.R.K.; Ehlke, B.; Le Maguerès, P.; Reinheimer, E.W.; Song, X.; Fei, H.; Oliver, S.R.J. Structural Diversity of Four Lanthanide Metal–Organic Frameworks Based on 2,6-Naphthalenedicarboxylate: Synthesis, Structures and Photoluminescent Properties. *Cryst. Eng. Comm.* **2021**, *23*, 1388–1397. [CrossRef]
15. Ying, C. Metal-Organic Framework as a New Photocatalyst for Environmental Pollutant Treatment. *Conf. Ser. Earth Environ.* **2021**, *631*, 012021-29. [CrossRef]

16. Zango, Z.U.; Jumbri, K.; Sambudi, N.S.; Ramli, A.; Abu Bakar, N.H.; Saad, B.; Rozaini, M.N.; Isiyaka, H.A.; Jagaba, A.H.; Aldaghri, O.; et al. A Critical Review on Metal-Organic Frameworks and Their Composites as Advanced Materials for Adsorption and Photocatalytic Degradation of Emerging Organic Pollutants from Wastewater. *Polymers* **2020**, *11*, 2648. [CrossRef]
17. Son, F.A.; Atilgan, A.; Idrees, K.B.; Islamoglu, T.; Farha, O.K. Solvent-Assisted Linker Exchange Enabled Preparation of Cerium-Based Metal–Organic Frameworks Constructed from Redox Active Linkers. *Inorg. Chem. Front.* **2020**, *7*, 984–990. [CrossRef]
18. Stawowy, M.; Róziewicz, M.; Szczepańska, E.; Silvestre-Albero, J.; Zawadzki, M.; Musioł, M.; Łuzny, R.; Kaczmarczyk, J.; Trawczyński, J.; Łamacz, A. The Impact of Synthesis Method on the Properties and CO_2 Sorption Capacity of UiO-66(Ce). *Catalysts* **2019**, *4*, 309. [CrossRef]
19. Yang, S.; Shen, H.; Cheng, F.; Wu, C.; Cao, Y.; Zhuo, S.; Zhang, Q.; Zhang, H. Organometallic Precursor Induced Defect-Enriched Mesoporous CeO_2 with High Specific Surface Area: Preparation and Catalytic Performance. *J. Mater. Chem. A* **2020**, *8*, 14006–14014. [CrossRef]
20. Lammert, M.; Wharmby, M.T.; Bueken Smolders, B.; Lieb, A.; Lomachenko, K.A.; Vos, D.D.; Stock, N. Cerium-Based Metal Organic Frameworks with UiO-66 Architecture: Synthesis, Properties and Redox Catalytic Activity. *Chem. Commun.* **2015**, *51*, 12578–12581. [CrossRef]
21. Taddei, M.; Dau, P.V.; Cohen, S.M.; Ranocchiari, M.; Van Bokhoven, J.A.; Costantino, F.; Vivani Sabatini, R. Efficient Microwave Assisted Synthesis of Metal–Organic Framework UiO-66: Optimization and Scale Up. *Dalton Trans.* **2015**, *44*, 14019–14026. [CrossRef]
22. Ezzatpour Ghadim, E.; Walker, M.; Walton, R.I. Rapid Synthesis of Cerium-UiO-66 MOF Nanoparticles for Photocatalytic Dye Degradation. *Dalton Trans.* **2023**, *52*, 11143–11157. [CrossRef]
23. Lammert, M.; Glißmann, C.; Stock, N. Tuning the Stability of Bimetallic Ce(IV)/Zr(IV)-Based MOFs with UiO-66 and MOF-808 Structures. *Dalton Trans.* **2017**, *46*, 2425–2429. [CrossRef]
24. Parnicka, P.; Lisowski, W.; Klimczuk, T.; Mikolajczyk, A.; Zaleska-Medynska, A. A Novel (Ti/Ce)UiO-X MOFs@TiO_2 Heterojunction for Enhanced Photocatalytic Performance: Boosting Via Ce^{4+}/Ce^{3+} and Ti^{4+}/Ti^{3+} Redox Mediators. *Appl. Catal. B* **2022**, *310*, 121349. [CrossRef]
25. Kim, H.; Kim, D.; Moon, D.; Choi, Y.N.; Baek, S.B.; Lah, M.S. Symmetry-Guided Syntheses of Mixed-Linker Zr Metal–Organic Frameworks with Precise Linker Locations. *Chem. Sci.* **2019**, *10*, 5801–5806. [CrossRef]
26. Butova, V.V.; Budnyk, A.P.; Charykov, K.M.; Vetlitsyna-Novikova, K.S.; Bugaev, A.L.; Guda, A.A.; Damin, A.; Chavan, S.M.; Øien-Ødegaard, S.; Lillerud, K.P.; et al. Partial and Complete Substitution of the 1,4-Benzenedicarboxylate Linker in UiO-66 with 1,4-Naphthalenedicarboxylate: Synthesis, Characterization, and H_2-Adsorption Properties. *Inorg. Chem.* **2019**, *58*, 1607–1620. [CrossRef]
27. Butova, V.V.; Burachevskaya, O.A.; Ozhogin, I.V.; Borodkin, G.S.; Starikov, A.G.; Bordiga, S.; Damin, A.; Lillerud, K.P.; Soldatov, A.V. UiO-66 Type MOFs with Mixed-Linkers 1,4-Benzenedicarboxylate and 1,4-Naphthalenedicarboxylate: Effect of the Modulator and Post-Synthetic Exchange. *Microporous Mesoporous Mater.* **2020**, *305*, 110324. [CrossRef]
28. Wang, A.; Zhou, Y.; Wang, Z.; Chen, M.; Sun, L.; Liu, X. Titanium Incorporated with UiO-66(Zr)-Type Metal–Organic Framework (MOF) for Photocatalytic Application. *RSC Adv.* **2016**, *6*, 3671–3679. [CrossRef]
29. Xia, H.-L.; Zhou, K.; Guo, J.; Zhang, J.; Huang, X.; Luo, D.; Liu, X.-Y.; Li, J. Amino Group Induced Structural Diversity and near-Infrared Emission of Yttrium-Tetracarboxylate Frameworks. *Chem. Sci.* **2020**, *13*, 9321–9328. [CrossRef]
30. Nasalevich, M.A.; Hendon, C.H.; Santaclara, J.G.; Svane, K.; van der Linden, B.; Veber, S.L.; Fedin, M.V.; Houtepen, A.J.; van der Veen, M.A.; Kapteijn, F.; et al. Electronic Origins of Photocatalytic Activity in D0 Metal Organic Frameworks. *Sci. Rep.* **2016**, *6*, 23676. [CrossRef]
31. Makuła, P.; Pacia, M.; Macyk, W. How to Correctly Determine the Band Gap Energy of Modified Semiconductor Photocatalysts Based on UV–Vis Spectra. *J. Phys. Chem. Lett.* **2018**, *9*, 6814–6817. [CrossRef]
32. Flage−Larsen, E.; Røyset, A.; Cavka, J.H.; Thorshaug, K. Band Gap Modulations in UiO Metal–Organic Frameworks. *J. Phys. Chem. C* **2013**, *117*, 20610–20616. [CrossRef]
33. Yasin, A.S.; Li, J.; Wu, N.; Musho, T. Study of the Inorganic Substitution in a Functionalized UiO-66 Metal–Organic Framework. *Phys. Chem. Chem. Phys.* **2016**, *18*, 12748–12754. [CrossRef]
34. Hou, W.; Chen, C.; Wang, Y.; Xu, Y. Cerium Versus Zirconium UiO-66 Metal–Organic Frameworks Coupled with CdS for H_2 Evolution under Visible Light. *Catal. Sci. Technol.* **2022**, *12*, 4012–4019. [CrossRef]
35. Nasalevich, M.A.; Goesten, M.G.; Savenije, T.J.; Kapteijn, F.; Gascon, J. Enhancing Optical Absorption of Metal–Organic Frameworks for Improved Visible Light Photocatalysis. *Chem. Commun.* **2013**, *49*, 10575–10577. [CrossRef]
36. Wasson, M.C.; Xie, H.; Wang, X.; Duncan, J.S.; Farha, O.K. Structural Transformation of Metal Oxo Species within UiO-66 Type Metal–Organic Frameworks. *Cryst. Eng. Comm.* **2022**, *24*, 5135–5140. [CrossRef]
37. Shearer, G.C.; Chavan, S.; Ethiraj, J.; Vitillo, J.G.; Svelle, S.; Lamberti, C.; Olsbye, U.; Bordiga, S.; Lillerud, K.P. Tuned to Perfection: Ironing out the Defects in Metal–Organic Framework UiO-66. *Chem. Mater.* **2014**, *26*, 4068–4071. [CrossRef]
38. Tan, K.; Pandey, H.; Wang, H.; Velasco, E.; Wang, K.-Y.; Zhou, H.-C.; Li, J.; Thonhauser, T. Defect Termination in the UiO-66 Family of Metal–Organic Frameworks: The Role of Water and Modulator. *J. Am. Chem. Soc.* **2021**, *143*, 6328–6332. [CrossRef]
39. Atzori, C.; Shearer, G.C.; Maschio, L.; Civalleri, B.; Bonino, F.; Lamberti, C.; Svelle, S.; Lillerud, K.P.; Bordiga, S. Effect of Benzoic Acid as a Modulator in the Structure of UiO-66: An Experimental and Computational Study. *J. Phys. Chem. C* **2017**, *121*, 9312–9324. [CrossRef]

40. Zhang, Y.; Chen, H.; Pan, Y.; Zeng, X.; Jiang, X.; Long, Z.; Hou, X. Cerium-Based UiO-66 Metal–Organic Frameworks Explored as Efficient Redox Catalysts: Titanium Incorporation and Generation of Abundant Oxygen Vacancies. *Chem. Commun.* **2019**, *55*, 13959–13962. [CrossRef]
41. Valenzano, L.; Civalleri, B.; Chavan, S.; Bordiga, S.; Nilsen, M.H.; Jakobsen, S.; Lillerud, K.P.; Lamberti, C. Disclosing the Complex Structure of UiO-66 Metal Organic Framework: A Synergic Combination of Experiment and Theory. *Chem. Mater.* **2011**, *23*, 1700–1718. [CrossRef]
42. Han, Y.; Liu, M.; Li, K.; Sun, Q.; Zhang, W.; Song, C.; Zhang, G.; Zhang, Z.C.; Guo, X. In Situ Synthesis of Titanium Doped Hybrid Metal–Organic Framework UiO-66 with Enhanced Adsorption Capacity for Organic Dyes. *Inorg. Chem. Front.* **2017**, *4*, 1870–1880. [CrossRef]
43. Huo, L.; Wang, L.; Li, J.; Pu, Y.; Xuan, K.; Qiao, C.; Yang, H. Cerium Doped Zr-Based Metal-Organic Framework as Catalyst for Direct Synthesis of Dimethyl Carbonate from CO_2 and Methanol. *J. CO2 Util.* **2023**, *68*, 102352. [CrossRef]
44. Han, Y.; Liu, M.; Li, K.; Zuo, Y.; Wei, Y.; Xu, S.; Zhang, G.; Song, C.; Zhang, Z.; Guo, X. Facile Synthesis of Morphology and Size-Controlled Zirconium Metal–Organic Framework UiO-66: The Role of Hydrofluoric Acid in Crystallization. *Cryst. Eng. Comm.* **2015**, *17*, 6434–6440. [CrossRef]
45. Jin, L.; Liu, H.; Xu, A.; Wu, Y.; Lu, J.; Liu, J.; Xie, S.; Yao, Y.; Dong, L.; Zhang, M.; et al. Defective UiO-66-NH_2 (Zr/Ce) Catalyses the Synthesis of Propylene Carbonate under Mild Conditions. *Microporous Mesoporous Mater.* **2021**, *317*, 110997. [CrossRef]
46. Jiao, Y.; Liu, Y.; Zhu, G.; Hungerford, J.T.; Bhattacharyya, S.; Lively, R.P.; Sholl, D.S.; Walton, K.S. Heat-Treatment of Defective UiO-66 from Modulated Synthesis: Adsorption and Stability Studies. *J. Phys. Chem. C* **2017**, *121*, 23471–23479. [CrossRef]
47. Mu, X.; Jiang, J.; Chao, F.; Lou, Y.; Chen, J. Ligand Modification of UiO-66 with an Unusual Visible Light Photocatalytic Behavior for RhB Degradation. *Dalton Trans.* **2018**, *46*, 1895–1902. [CrossRef]
48. Piscopo, C.G.; Trapani, F.; Polyzoidis, A.; Schwarzer, M.; Pace, A.; Loebbecke, S. Positive Effect of the Fluorine Moiety on the Oxygen Storage Capacity of UiO-66 Metal–Organic Frameworks. *New J. Chem.* **2016**, *46*, 8220–8224. [CrossRef]
49. Caruso, T.; Bedini, E.; De Castro, C.; Parrilli, M. Brønsted Acidity of Ceric Ammonium Nitrate in Anhydrous DMF. The Role of Salt and Solvent in Sucrose Cleavage. *Tetrahedron* **2006**, *62*, 2350–2356. [CrossRef]
50. Hong, D.; Murakami, M.; Yamada, Y.; Fukuzumi, S. Efficient Water Oxidation by Cerium Ammonium Nitrate with [Ir III(CP*)(4,4′-Bishydroxy-2,2′-Bipyridine)(H_2O)]$^{2+}$ as a Precatalyst. *Energy. Environ. Sci.* **2012**, *5*, 5708–5716. [CrossRef]
51. Tu, J.; Zeng, X.; Xu, F.; Wu, X.; Tian, Y.; Hou, X.; Long, Z. Microwave-Induced Fast Incorporation of Titanium into UiO-66 Metal–Organic Frameworks for Enhanced Photocatalytic Properties. *Chem. Commun.* **2017**, *53*, 3361–3364. [CrossRef] [PubMed]
52. Fang, X.; Wu, S.; Wu, Y.; Yang, W.; Li, Y.; He, J.; Hong, P.; Nie, M.; Xie, C.; Wu, Z.; et al. High-efficiency adsorption of norfloxacin using octahedral UiO-66-NH_2 nanomaterials: Dynamics, thermodynamics, and mechanism. *Appl. Surf. Sci.* **2020**, *518*, 146226. [CrossRef]
53. Chen, H.; Liu, C.; Guo, W.; Wang, Z.; Shi, Y.; Yu, Y.; Wu, L. Functionalized UiO-66(Ce) for photocatalytic organic transformation: The role of active sites modulated by ligand functionalization. *Catal. Sci. Technol.* **2022**, *12*, 1812–1823. [CrossRef]
54. Wang, F.; Xue, R.; Yujie, M.; Ge, Y.; Wang, Z.; Qiao, X.; Zhou, P. Study on the Performance of a MOF-808-Based Photocatalyst Prepared by a Microwave-Assisted Method for the Degradation of Antibiotics. *RSC Adv.* **2021**, *11*, 32955–32964. [CrossRef] [PubMed]
55. Ibrahim, A.H.; El-Mehalmey, W.A.; Haikal, R.R.; Safy, M.E.A.; Amin, M.; Shatla, H.R.; Karakalos, S.G.; Alkordi, M.H. Tuning the Chemical Environment within the UiO-66-NH_2 Nanocages for Charge-Dependent Contaminant Uptake and Selectivity. *Inorg. Chem.* **2019**, *58*, 15078–15087. [CrossRef] [PubMed]
56. Feng, L.; Yuan, S.; Zhang, L.; Tan, K.; Li, J.-L.; Kirchon, A.; Liu, L.-M.; Zhang, P.; Han, Y.; Chabal, Y.J.; et al. Creating Hierarchical Pores by Controlled Linker Thermolysis in Multivariate Metal–Organic Frameworks. *J. Am. Chem. Soc.* **2018**, *140*, 2363–2372. [CrossRef] [PubMed]
57. Zhao, D.; Cai, C. Cerium-Based UiO-66 Metal-Organic Framework for Synergistic Dye Adsorption and Photodegradation: A Discussion of the Mechanism. *Dyes Pigm.* **2021**, *185*, 108957. [CrossRef]
58. Rego, R.M.; Sriram, G.; Ajeya, K.V.; Jung, H.-Y.; Kurkuri, M.D.; Kigga, M. Cerium Based UiO-66 MOF as a Multipollutant Adsorbent for Universal Water Purification. *J. Hazard. Mater.* **2021**, *416*, 125941. [CrossRef]
59. Sun, D.; Liu, W.; Qiu, M.; Zhang, Y.; Li, Z. Introduction of a Mediator for Enhancing Photocatalytic Performance Via Post-Synthetic Metal Exchange in Metal–Organic Frameworks (MOFs). *Chem. Commun.* **2015**, *51*, 2056–2059. [CrossRef]
60. DeStefano, M.R.; Islamoglu, T.; Garibay, S.J.; Hupp, J.T.; Farha, O.K. Room-Temperature Synthesis of UiO-66 and Thermal Modulation of Densities of Defect Sites. *Chem. Mater.* **2017**, *29*, 1357–1361. [CrossRef]
61. Xia, Q.; Yu, X.; Zhao, H.; Wang, S.; Wang, H.; Guo, Z.; Xing, H. Syntheses of Novel Lanthanide Metal–Organic Frameworks for Highly Efficient Visible-Light-Driven Dye Degradation. *Cryst. Growth Des.* **2017**, *17*, 4189–4195. [CrossRef]
62. Li, Y.; Lin, B.; Ge, L.; Guo, H.; Chen, X.; Lu, M. Real-Time Spectroscopic Monitoring of Photocatalytic Activity Promoted by Graphene in a Microfluidic Reactor. *Sci. Rep.* **2016**, *6*, 28803. [CrossRef] [PubMed]
63. Bhoi, Y.P.; Pradhan, S.R.; Behera, C.; Mishra, B.G. Visible Light Driven Efficient Photocatalytic Degradation of Congo Red Dye Catalyzed by Hierarchical CuS–$Bi_2Cu_XW_{1-X}O_{6-2X}$ Nanocomposite System. *RSC Adv.* **2016**, *46*, 35589–35601. [CrossRef]
64. Sood, S.; Mehta, S.K.; Umar, A.; Kansal, S.K. The Visible Light-Driven Photocatalytic Degradation of Alizarin Red S Using Bi-Doped TiO_2 Nanoparticles. *New J. Chem.* **2014**, *46*, 3127–3136. [CrossRef]

65. Toby, B.H.; Von Dreele, R.B. GSAS-II: The Genesis of a Modern Open-Source All Purpose Crystallography Software Package. *J. Appl. Crystallogr.* **2013**, *46*, 544–549. [CrossRef]
66. Fairley, N.; Fernandez, V.; Richard-Plouet, M.; Guillot-Deudon, C.; Walton, J.; Smith, E.; Greiner Flahaut, M.; Biesinger, M.; Tougaard, S.; Morgan, D. Baltrusaitis. *Appl. Surf. Sci.* **2021**, *5*, 100112. [CrossRef]
67. Zhang, J.; Li, F.; Sun, Q. Rapid and Selective Adsorption of Cationic Dyes by a Unique Metal-Organic Framework with Decorated Pore Surface. *Appl. Surf. Sci.* **2018**, *440*, 1219–1226. [CrossRef]
68. Revellame, E.D.; Fortela, D.L.; Sharp, W.; Hernandez, R.; Zappi, M.E. Adsorption Kinetic Modelling Using Pseudo-First Order and Pseudo-Second Order Rate Laws: A Review. *Clean. Eng. Technol.* **2020**, *1*, 100032. [CrossRef]